Available online at www.sciencedirect.com

ScienceDirect

Geochimica et Cosmochimica Acta 190 (2016) 213–238

Geochimica et Cosmochimica Acta

www.elsevier.com/locate/gca

Hydrothermal versus active margin sediment supply to the eastern equatorial Pacific over the past 23 million years traced by radiogenic Pb isotopes: Paleoceanographic and paleoclimatic implications

Tobias W. Höfig *, Kaj Hoernle, Folkmar Hauff, Martin Frank

GEOMAR Helmholtz Centre for Ocean Research Kiel, Wischhofstr. 1-3, D-24148 Kiel, Germany

Received 15 July 2015; accepted in revised form 1 May 2016; Available online 7 May 2016

Abstract

We investigated the evolution of the Pb isotopic composition of bulk sediments on the Cocos Plate in sedimentary successions of Deep Sea Drilling Project (DSDP) Site 495 and Ocean Drilling Program/Integrated Ocean Drilling Program (ODP/IODP) Site 1256 over the past 23 million years of depositional history. Our study addresses the relationship of the sediment Pb isotope record to plate tectonics, weathering inputs, and paleoceanography. It is the first effort to characterize the Pb isotopic evolution of eastern equatorial Pacific sedimentation covering the entire tectonic pathway of the Cocos Plate from its formation at the East Pacific Rise to its arrival at the Central American subduction zone. The Sites 495 and 1256 bulk sediment Pb isotope records are fully consistent over time despite distinct differences between the type of sediment deposited at both locations. A systematic and continuous trend from ~23 to ~6–4 Ma toward more radiogenic Pb isotopic compositions, e.g., $^{206}Pb/^{204}Pb$ ratios increase from 18.29 to 18.81, reflects a decrease in the contribution of hydrothermal particles from the East Pacific Rise and an increase in the predominantly eolian contribution of mixed weathering products from the continental arcs of the Northern and south Central Andes as well as from southern Mexico. Surprisingly, both the Pb isotopic composition of the detrital fraction and that of past seawater indicate that inputs from nearby Central America and the Galápagos Archipelago did not significantly contribute to the sediments of our core locations but were overwhelmed by other sediment sources. A systematic change to less radiogenic Pb isotope ratios in sediments younger than ~4–3 Ma, reaching present-day $^{206}Pb/^{204}Pb$ values near 18.70, reflects a reduction of the continental input from the South Central Volcanic Zone of the Andean Arc and increased contributions from southern Mexican igneous complexes. This isotopic trend reversal took place as a consequence of changes in atmospheric circulation, when the studied sites crossed the Intertropical Convergence Zone due to tectonic drift and concurrent climate cooling. Eolian transport has played a major role in the supply of detrital material over the entire Neogene and Quaternary. The delivery of hydrothermal Pb originating from the East Pacific Rise to the easternmost tropical Pacific has been a persistent feature that is attributed to a remarkably stable central and eastern Pacific deep-water flow pattern over millions of years. Thus, deep ocean circulation did not change significantly either (1) as a consequence of an Early Miocene closure of the deep gateway between the Caribbean and eastern Central Pacific or because (2) a Late Miocene to Pliocene closure of the Central American Seaway had no impact at all.

Keywords: IODP Site 1256; DSDP Site 495; Marine sediments; Pb isotopes; Cocos Plate; Eastern equatorial Pacific

* Corresponding author at: Department of Mineralogy, TU Bergakademie Freiberg, Brennhausgasse 14, D-09599 Freiberg, Germany

http://dx.doi.org/10.1016/j.gca.2016.05.003

1. INTRODUCTION

Lead (Pb) isotopes have served as a powerful tool for tracking the source regions of oceanic water masses (e.g., O'Nions et al., 1978; von Blanckenburg et al., 1996; Abouchami et al., 1997; Frank et al., 1999; van de Flierdt et al., 2004a,b; Ling et al., 2005; Haley et al., 2008) and of detrital sediments (e.g., Chow and Patterson, 1962; Jones et al., 2000; Pettke et al., 2000, 2002; Godfrey, 2002; Stancin et al., 2006; Xie and Marcantonio, 2012; Basak and Martin, 2013; Pichat et al., 2014; Wilson et al., 2015) on different time scales. The importance of dissolved Pb isotopes as an oceanographic tracer for continental inputs arises from the low mean deep-water oceanic residence time of dissolved Pb of ~50 (Atlantic) to ~200–400 (Pacific) years (Schaule and Patterson, 1981; von Blanckenburg and Igel, 1999), being considerably shorter than the global ocean mixing time of ~1500 years (e.g., Broecker et al., 1982). Since there are three radiogenic Pb isotopes, they allow detailed reconstructions of complex mixing relationships between different isotopic source end-members within the same isotopic system (cf. Frank, 2002; Goldstein and Hemming, 2003). Variations in the Pb isotopic composition of different phases of marine sediments thus provide an important archive for reconstructing both tectonically and climatically driven changes in sediment provenance and in the signatures of water masses transporting the particulate or dissolved Pb through time.

In the eastern equatorial Pacific Ocean (EEP), possible sedimentary source materials include (1) tephras released from the Galápagos Hotspot and the Mexican, Central American, and Andean subduction zone volcanoes, (2) particulate matter originating from expelled hydrothermal fluids associated with areas of active submarine volcanism at the East Pacific Rise and at the Galápagos (or Cocos-Nazca) spreading centers, as well as Galápagos volcanoes, and (3) detrital (riverine and airborne) inputs derived from weathering and erosion of the surrounding active continental margins (Fig. 1). Changes in the proportions of these contributing sources bear important information on the climatic and tectonic evolution of the EEP, which can be reconstructed from the detrital Pb isotopic compositions of EEP sediments. To date, only few such studies have been carried out. Following the pioneering work of Nakai et al. (1993), who investigated Sr–Nd isotopic compositions of the eolian detrital fraction of Late Pleistocene EEP sediments to constrain its source areas, Jones et al. (2000) concluded from detrital Pb isotope distributions that dust supply of South American origin

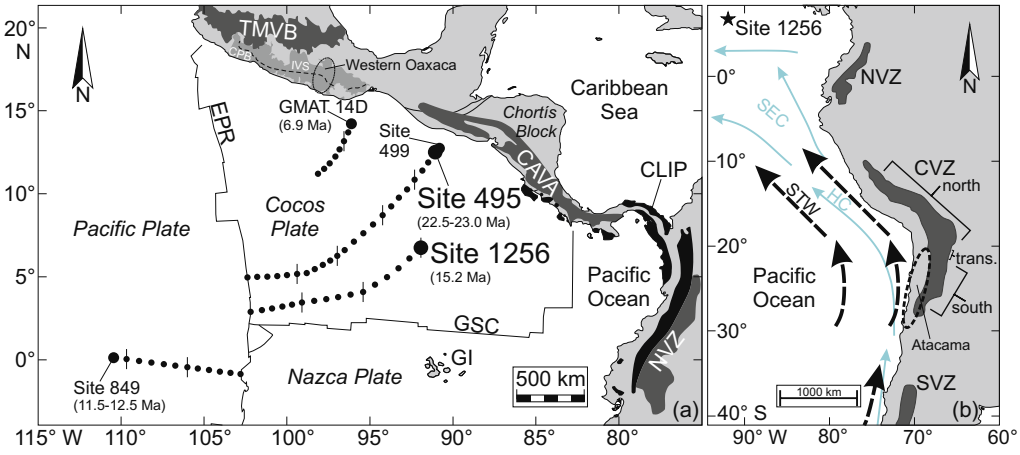

Fig. 1. (a) Map of the eastern equatorial Pacific and adjacent continental areas, showing the locations of the studied ocean drilling sites 495 and 1256 together with other oceanic locations referred to in the text (Fe–Mn crust GMAT 14D; drilling sites 499, 849). Indicated oceanic crustal ages of drilling site locations are based on magnetic lineations (Sites 495, 499: von Huene et al., 1982; Geldmacher et al., 2013; Sites 849, 1256: Wilson, 1996) according to the geomagnetic polarity time scale of Cande and Kent (1995). The age of Fe–Mn crust GMAT 14D is derived from Frank et al. (1999). Reconstructed tectonic tracks were calculated with the software GPlates (http://www.gplates.org; version 1.1.1). Small dots along the tracks mark 1 Ma and small ticks label 5 Ma increments. Spreading ridges: EPR = East Pacific Rise, GSC = Galápagos Spreading Center (Cocos-Nazca Spreading Center). Other oceanic/continental geological entities: CAVA = Central American Volcanic Arc, CLIP = Caribbean Large Igneous Province (uplifted parts), CPB = Coastal Plutonic Belt, GI = Galápagos Islands, IVS = Inland Volcanic Sequences, NVZ = Northern (Andean) Volcanic Zone, TMVB = Trans-Mexican Volcanic Belt. Simplified boundary between Cenozoic IVS and CPB in southern Mexico modified from Morán-Zenteno et al. (1999). The dashed ellipse marks the western Oaxaca area studied by Martiny et al. (2000) who produced Pb isotope data used for comparison with the data set of the present study. Chortís Block tectonic boundaries after Rogers et al. (2007). (b) Map of the easternmost tropical and southeastern Pacific and adjacent western part of South America [adapted from Hart and Miller (2006), including oceanic circulation data from Kessler (2006)], depicting major present-day ocean surface (turquoise arrows) and wind (dashed black arrows) currents affecting this area: HC = Humboldt Current, SEC = South Equatorial Current, STW = Southeast Trade Winds. In addition, major volcanic zones of the Andes including the Atacama Desert are displayed: NVZ = Northern Volcanic Zone, CVZ = Central Volcanic Zone (north, transitional (trans.), south; cf. Pichat et al., 2014), SVZ = Southern Volcanic Zone. Note that the Austral Volcanic Zone, being the southernmost Andean Arc segment, follows south of the SVZ (i.e., from 49° to 55°S), thus outside the shown map. Site 1256 location is marked by a black star.

dominates the EEP, however, without further source specification. Based on statistical analysis of detrital Sr–Nd–Pb isotope distributions, Stancin et al. (2006) showed that Pacific detritus of the past 5 Ma has been dominated by three major continental components derived from Asia, North America, and Central/South America, with predominance of the latter source in the EEP east of ~100°W. In addition, North Africa (Sahara) and Australia could not be excluded as potential dust sources for young (⩽25 ka) eolian sediments retrieved along ~110°W between ~7°N and ~3°S (Xie and Marcantonio, 2012). However, Pichat et al. (2014) recently found no significant Pb isotopic evidence for input from such distal sources in eolian-dominated bulk sediments of the same meridional transect during the past 160 ka. Instead, these authors provided clear isotopic fingerprints, which demonstrated that Late Pleistocene to Holocene equatorial dust deposition at ~110°W has been controlled by South American detrital input derived from erosion of volcanic arc segments of the Central and Southern Andes and has been supplied by the Southeast Trade Winds over the entire investigated period of time.

It remains to be shown how these inputs evolved on longer time scales covering major global and local tectonic and climatic changes, such as global Cenozoic cooling, the onset of Northern Hemisphere glaciation and the associated increase in wind speeds and wind transport (e.g., Rea, 1994). An additional challenge in deciphering the origin of detrital input is the northeastward tectonic movement of the Cocos Plate leading to spatial changes in sedimentary facies over time at a single site. Furthermore, it is not clear how the source-pathway system evolved in the easternmost part of the tropical Pacific, which moved ~2000 km closer to Central America into much stronger influence of hemipelagic sediment supply (i.e., continental shelf, riverine; cf. Rea, 1994) over the past 23 million years.

Here we reconstruct the Pb isotopic evolution of bulk sediments from Deep Sea Drilling Project (DSDP) Site 495 and Ocean Drilling Program/Integrated Ocean Drilling Program (ODP/IODP) Site 1256. Together they cover ~23 million years of marine sedimentation on the Cocos Plate, which formed by the break-up of the Farallon Plate ~23 Ma ago (Handschumacher, 1976). The presented new Pb isotope data provide an unprecedented record of hydrothermal and detrital material supply in the eastern equatorial Pacific. We document changes in tectonically, climatically, and oceanographically driven detrital sedimentation along the entire pathway of the Cocos Plate from the spreading center at the East Pacific Rise to the Central American subduction zone. Thus, through deciphering the detrital provenance of marine sediments over time, the present study reinforces independent evidence for major consequences of global Neogene cooling in the eastern equatorial Pacific. Moreover, new constraints are provided on EEP deep-water circulation through time via changes in the abundance of particles formed by mid-ocean ridge hydrothermal activity in the eastern tropical Pacific Ocean, which allows insights into long-range hydrothermal dispersion processes.

2. BACKGROUND

2.1. Geological setting

DSDP Site 495 (12°29.8′N, 91°2.3′W) and ODP/IODP Site 1256 (6°44.2′N, 91°56.1′W) are located in the Guatemala Basin on the Cocos Plate ~700 km apart from each other (Fig. 1a). As inferred from marine magnetic anomalies, the oceanic basement at Site 495 formed 23–22.5 Ma ago (von Huene et al., 1982; Geldmacher et al., 2008, 2013) and the underlying seafloor of Site 1256 formed at ~15.2 Ma (Wilson, 1996).

The 428 m thick sediment succession at Site 495 was recovered during DSDP Leg 67 (Coulbourn et al., 1982) on a horst 22 km seaward of the Guatemala Trench axis in a water depth of 4140 m. The lower part of the Site 495 sediment column is characterized by a 251 m thick succession of Early to Middle Miocene calcareous oozes and chalks with precipitates of Fe–Mn minerals and chert at the bottom of the section. The upper 177 m of the sediment column comprise Late Miocene to Quaternary hemipelagic mud, containing primarily diatoms and radiolarians with subordinate tephra particles and brown abyssal clays (von Huene et al., 1982).

The 250 m thick sediment cover at Site 1256 was drilled at a water depth of 3635 m during ODP Leg 206, ~830 km to the WSW of Costa Rica (Wilson et al., 2003). The oceanic crust at Site 1256 was formed near the equator within the equatorial high-productivity zone leading to a high sedimentation rate of ~39 m/Ma in mid-Miocene times (Wilson et al., 2003; Jiang and Wise, 2007). The basal unit of the sediment section comprises 210 m of pelagic biogenic ooze, consisting of calcareous nannofossils with intercalations of diatom ooze (Wilson et al., 2003). As the site moved away from the equator, the amount of carbonate in the sediment decreased, whereas the relative proportion of clastic material increased. Consequently, the upper unit at Site 1256 comprises 40 m of terrigenous silty clay with varying minor amounts of biogenic particles and disseminated volcanic glass shards (Wilson et al., 2003). The initiation of this terrigenous-dominated sedimentation at ~5.5 Ma roughly corresponds to the Miocene–Pliocene boundary (Jiang and Wise, 2007).

Both sites have migrated toward Central America at rates of 7–9 cm/a (DeMets et al., 1990) as a result of northeastward motion of the Cocos Plate, which has been subducted beneath southern Mexico and Central America. The connection between plate tectonics and paleoceanographic processes in the study area comprises the evolution of the Central American Seaway, which linked the tropical western Atlantic and eastern Pacific throughout most of the Cenozoic and began to close in the Early to Middle Miocene with final closure at ~4–3 Ma (reviewed by Molnar, 2008). Seaway closing resulted from convergence of Central America (Panama) with NW South America (Farris et al., 2011) and from the collision and subduction of the Cocos Ridge, a part of the Galápagos Hotspot track, with southern Central America (Hoernle et al., 2002). However, the exact timing of closure and the evolution of the water depth of the seaway are still under debate in view of recent tec-

tonic reconstructions favoring disappearance of the deep oceanic gateway as early as ~15–13 Ma (Farris et al., 2011; Montes et al., 2012a, 2012b, 2015). Concurrently, Coates and Stallard (2013) have suggested that both scenarios of closure timing reflect different perceptions on the Central American Volcanic Arc evolution in terms of the geotectonic, biogeographic, and oceanic settings that developed during isthmus formation.

2.2. Atmospheric circulation

The Northeast and Southeast Trade Winds (N/STW; Fig. 2a) have governed the atmospheric circulation above the eastern equatorial Pacific and meet at the Intertropical Convergence Zone (ITCZ; Fig. 2a), which is currently located at a mean latitude of ~5°N (Rea, 1994; Hovan, 1995). At present, the ITCZ experiences considerable seasonal latitudinal shifts (between ~4 and ~10°N; Fig. 2a) ultimately controlled by the seasonally changing vigor of atmospheric circulation and thus of the trade winds in each hemisphere, which are on average stronger in the south as a consequence of the higher pole-equator temperature gradient in that hemisphere (e.g., Flohn, 1981; Hovan, 1995). As demonstrated by several studies (e.g., Rea, 1994; Hovan, 1995; Pettke et al., 2002; Hyeong et al., 2005), the Pacific ITCZ position was located considerably north of ~5°N prior to ~4 Ma (Fig. 2a), owing to a larger temperature gradient between the hemispheres in the

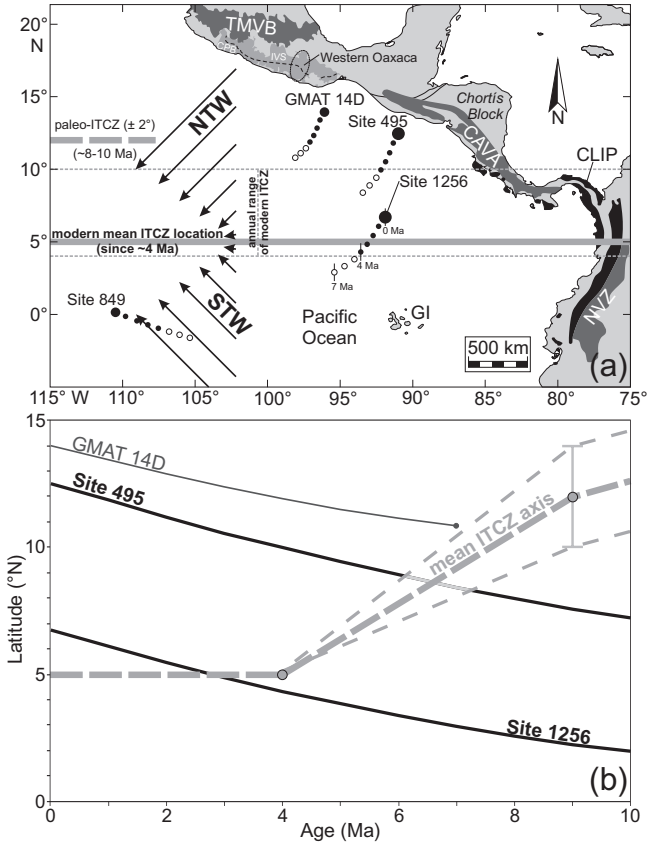

Fig. 2. (a) Map of the eastern equatorial Pacific, schematically showing simplified prevailing wind currents (adapted from Hovan, 1995) and the (present-day and Late Miocene) location of the Intertropical Convergence Zone (ITCZ). STW = Southeast Trade Winds, NTW = Northeast Trade Winds. Note that the wind pattern has a strong meridional component east of 110°W and is more complex and variable than indicated in the present figure (cf. Kessler, 2006). True paleopositions of considered drilling sites and Fe–Mn crust GMAT 14D are shown in 1 Ma increments from 7 Ma to the present (calculated with the software GPlates; http://www.gplates.org; version 1.1.1), corresponding to the growth period of GMAT 14D. Paleopositions represented by black dots (0–4 Ma) mark the period of time with the ITCZ being located at its average present-day latitude of ~5°N, showing an annual shift between ~4°N and ~10°N (dashed gray vertical line) (Rea, 1994; Hovan, 1995). The Late Miocene (~8–10 Ma) ITCZ location (Hyeong et al., 2005) is indicated by a thick dashed gray horizontal line. Declining relative wind strength with shorter distance to the ITCZ is schematically illustrated by decreasing length of simplified trade wind arrows in either atmospheric hemisphere (according to Wyrtki and Kilonsky, 1984). The indicated true paleopositions of oceanic sites refer to the real location of the associated ridge segment at a given point of time (see caption of Fig. 3 for further explanation). Ticks along the tectonic track of Site 1256 exemplarily mark 7, 4, and 0 Ma positions. Abbreviations are the same as in Fig. 1a. (b) Age (Ma) versus latitude (°N), reflecting the northward migration of eastern tropical Pacific drilling sites 495 and 1256 as well as Fe–Mn crust GMAT 14D over time, focusing on the past 10 million years. The plotted path of the southward shift of the average ITCZ axis (dashed gray line) during the Late Neogene has been estimated from interpolation between paleolocation of ~12 ± 2°N around 9 Ma (Hyeong et al., 2005) and current location of ~5°N established at ~4 Ma (Rea, 1994; Hovan, 1995). Note that the ITCZ was located even further north during the Early Neogene and Late Paleogene, respectively, probably being around 22°N at ~25 Ma (Rea, 1994).

unipolar world of the Neogene (Flohn, 1981), and then migrated southward to its current location. Consequently, the studied drilling sites on the northeastward moving Cocos Plate have been affected by different wind systems over time. While Site 1256 passed the average ITCZ position at ~3 Ma, Site 495 already crossed at ~7–6 Ma and has been subjected to the NTW since, as inferred from an estimate of the ITCZ migration path (Fig. 2b). In the study area, the wind pattern is, however, more complex than in the westerly part of the eastern equatorial Pacific, particularly with respect to the NTW (Kessler, 2006), which show pronounced meridional components instead of only strong latitudinal winds (see also Section 2.3).

The equatorial Pacific atmospheric circulation is weakest within the ITCZ and wind strength increases with distance from the ITCZ (Wyrtki and Kilonsky, 1984; Fig. 2a). However, despite the absence of strong winds, the ITCZ marks an area of enhanced eolian flux due to intense rainout of dust particles, thus efficiently preventing dust transfer between the hemispheres, particularly in the eastern Pacific (e.g., Rea, 1990, 1994; Hovan, 1995).

2.3. Oceanic circulation

The trade wind belts drive the oceanic surface circulation in the eastern equatorial Pacific. They force the equatorial waters in each hemisphere to flow westward (Fig. 3a), establishing the North Equatorial Current (NEC; north of the ITCZ) and the South Equatorial Current (SEC; south of the ITCZ) (e.g., review by

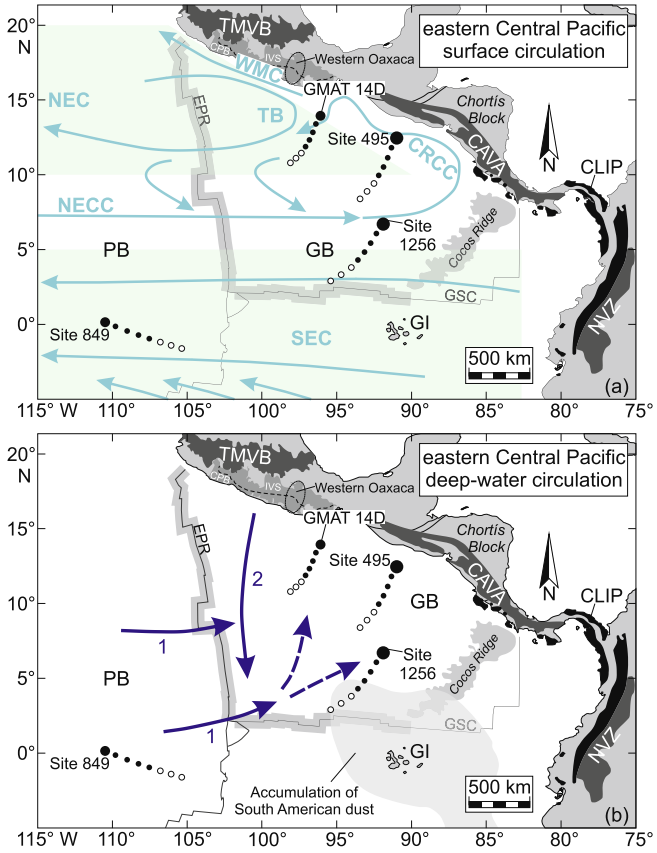

Fig. 3. Map of the eastern equatorial Pacific, schematically displaying major present-day lobes of (a) the oceanic surface [turquoise arrows; after Kessler (2006)] and (b) deep-water [continuous dark blue arrows: based on the studies by (1) Lonsdale (1976) and (2) Lyle (1992); dashed dark blue arrows: based on this study] current circulation affecting this area. Acronyms of surface currents: CRCC = Costa Rica Coastal Current, NEC = North Equatorial Current, NECC = North Equatorial Countercurrent, SEC = South Equatorial Current, TB = Tehuantepec Bowl, WMC = West Mexican Current. Pale blue, transparent marine areas delineate the latitudinal extent of the westward flowing NEC (north of ~10°N) and SEC (south of ~5°N) surface circulation system, respectively (Hovan, 1995). The submarine structural boundaries of the Guatemala Basin (GB) are highlighted in dark gray (Cocos Ridge and part of the EPR and GSC crests). PB = Pacific Basin. The northeast-tending, transparent, and light gray area crossing the GSC and extending up to ~5°N in (b) represents a sediment lobe suggested by Lyle (1992) as a result of eolian deposition via Southeast Trade Winds. True paleopositions of considered drill sites and Fe–Mn crust GMAT 14D are the same as in Fig. 2a. Along the tracks, black dots (0–4 Ma) mark the period of time, when the ITCZ has already been located at its average present-day latitude of ~5°N. Note that the true paleopositions of depicted drill sites (495, 849, 1256) and Fe–Mn crust GMAT 14D may deviate from the locations along the tectonic tracks shown in Fig. 1a, since the reconstruction of true paleopositions at a given age has taken into account that the associated ridge segment (e.g., EPR) has been subjected to ridge jumps through time. Thus, the reconstruction refers to the actual position of the corresponding ridge segment at a given point of time, which may be different from its present-day location. Abbreviations are the same as in Fig. 1a. (For interpretation of the references to color in this figure legend, the reader is referred to the web version of this article.)

Kessler, 2006). In between, the North Equatorial Countercurrent (NECC) flows eastward in the zone of weak winds (i.e., the ITCZ; Fig. 3a). The SEC is fed by the Humboldt Current (Kessler, 2006), which originates from offshore Chile and is deflected northwestward by the STW (García, 1994; Fig. 1b). The NEC controls the movement of eastern Pacific surface water masses north of ~10°N (Fig. 3a). The actual zonal westward surface flow, however, only starts west of ~120°W, since the easternmost tropical Pacific (i.e., the study area) is characterized by a more complex circulation pattern due to the collapse of the strictly zonal wind system and the establishment of weaker meridional (N–S directed) winds east of 110°W, which result in a gyre-like surface circulation and partially seasonally varying wind intensities (Kessler, 2006). This gives rise to a complex surface water circulation system in the Guatemala Basin mainly transporting water masses along N–S routes (Kessler, 2006), which contrasts with the SEC system operating south of ~5°N (Fig. 3a). There are two gyre-like surface water systems north of ~5°N, exchanging water masses and feeding the incoming NECC, which heads east toward southern Central America (Fig. 3a).

The abyssal circulation in the present-day central and eastern equatorial Pacific is characterized by latitudinal deep-water flow heading east toward the East Pacific Rise (Lonsdale, 1976, and references therein). It splits into two major bottom currents, most likely crossing the East Pacific Rise along transform faults just north of the Galápagos triple junction and at ~8°N (Fig. 3b). In addition, some of the deep-water body of the Guatemala Basin may be filled by diffuse overflow from the Pacific Basin across the ridge crest of the East Pacific Rise (Lonsdale, 1976). A second major flow direction constitutes a southward bottom current originating offshore southern Mexico and moving along the eastern flank of the East Pacific Rise (Lyle, 1992; Fig. 3b).

3. SAMPLE PREPARATION AND ANALYTICAL METHODS

The present study includes 32 samples covering the entire sediment column drilled at Site 1256 and 16 samples of Site 495. These samples were obtained from the Gulf Coast Repository at Texas A&M University (College Station, TX, USA). Distinct tephra layers were avoided during sampling in order to understand the long-term detrital source variations that were not obscured by short-term volcanic fallout derived from explosive events. Details of sample intervals, chronology, and lithology of the studied samples are provided in Table 1.

The bulk sediment samples, consisting of authigenic seawater-derived (e.g., calcareous ooze, Fe–Mn oxyhydroxide coatings) and continent-derived (e.g., terrigenous clay) components in varying proportions, were dried over 48 h at 50 °C and 0.8–1.2 g were taken for trace element and isotope analyses. On a subset of five bulk samples from Site 1256 (1.5–2.6 g each sample), leaching experiments following the procedure of Gutjahr et al. (2007) and modified by Stumpf et al. (2010) were carried out to separate the detrital and the authigenic seawater-derived Pb fractions. The latter are mainly contained in early diagenetic ferromanganese (Fe–Mn) coatings of the particles and have been shown to reliably reflect seawater Pb isotopic compositions (Gutjahr et al., 2009; Stumpf et al., 2010; Wilson et al., 2015). Basically, the leaching processes encompassed a two-day procedure including several shaking and centrifuging steps. First, carbonate was removed with a 20 ml solution of 15%-acetic acid/1 M-Na acetate buffer (pH of ~4.1 for 1 h), followed by a triple rinse with deionized water followed by addition of another 10 ml of the same acetate solution diluted with 10 ml of MQ water for overnight shaking (125 rot/min). Subsequently, a 0.05 M-hydroxylamine hydrochloride/15%-acetic acid solution buffered to pH of 3.6 with NaOH was added to dissolve the Fe–Mn coatings. After shaking for 1 h, the supernatant was pipetted into 30 ml Teflon® vials for further ion-chromatographic separation. The residual detrital material was then dried over 48 h at 50 °C. Although the 1.6 ng Pb blank for the leaching procedure is fairly high when compared to 0.006–0.075 ng Pb procedural blank of the unleached samples, the leaching blank is still considered negligible in light of the total amount of Pb extracted (1840–31,209 ng) during leaching. These observations and conclusions are consistent with those of Wilson et al. (2015).

About 100 to 200 mg of sample material from the 48 unleached bulk samples and the residues of the five leached samples were weighed into 15 ml Teflon beakers and dissolved in a 4:1 HF-HNO_3 mixture at 150 °C for 48 h with closed lids. No visible particles were observed in any of the samples after the dissolution procedure. After initial drying, the residue was converted to chloride form using 6 M HCl. In rare cases of precipitate formation, additional ultrasonic cleaning was applied until a clear solution was obtained. Pb ion-chromatography followed the two-pass column procedure of Hoernle and Tilton (1991) using 100 µl Teflon columns loaded with Bio-Rad AG 1X8 (100–200 mesh) resin equilibrated in 1 M HBr for maximum Pb retention and complete Pb release through a 1 ml wash-out in 6 M HCl.

Pb isotope analysis was carried out by thermal ionization mass spectrometry (TIMS) at GEOMAR on a Finnigan MAT 262 RPQ^{2+}, operating in static multi-collection mode. Within-run errors are reported as double standard error (2SE = double standard deviation (2SD)/$\sqrt{n-1}$ with n representing the number of scans passing the 2SD outlier test of all integrations). The external analytical reproducibility is reported as 2SD of repeated NBS981 analyses (Table 2). Since ^{204}Pb is the sole naturally occurring stable Pb isotope, mass bias correction was carried out applying a Pb double spike (Pb–DS) in order to obtain high precision Pb isotope ratios. Details of the technique applied in the TIMS facilities at GEOMAR are described in Hoernle et al. (2011) and are briefly summarized in the following. Basically, Pb–DS involves measurement of common and spiked Pb of a sample. The latter involves adding a ^{207}Pb–^{204}Pb spike to the sample in such amounts that an optimized sample to spike ratio monitored by $^{204}Pb/^{206}Pb = 0.5–2.0$ is achieved. The double spike has been calibrated against NBS982 using the certified $^{208}Pb/^{206}Pb = 1.000160$ (https://www-s.nist.gov/srmors/certArchive.cfm) as fixed ratio for internal

Table 1
Sample interval details, inferred biostratigraphic ages, lithology, and appropriate microfossil species used for age determinations of studied samples from both sediment cores. mbsf = meters below seafloor, FO = first occurrence, LO = last occurrence.

Site/hole	Core/section	Interval (cm)	Depth (mbsf)	Biostrati-graphic age estimate (Ma)	Appropriate linear sedimentation rate (m/Ma)*	Lithology†	Appropriate biohorizon, with mean depth and age, used for calculation of biostratigraphic ages	Reference for microfossil species	Reference for microfossil datum level
1256A	1H-1	32–34	0.32	0.04	11.8	Nannofossil silty clay with diatoms	LO *Pseudoemiliania lacunosa* (5.28 mbsf, 0.46 Ma)	Jiang and Wise (2007)	Berggren et al. (1995a)
1256A	1H-2	19–21	1.69	0.16	11.8	Nannofossil silty clay with diatoms			
1256B	1H-4	56–58	5.06	0.44	11.8	Nannofossil silty clay			
1256B	3H-2	34–36	17.44	1.76	6.1	Clayey nannofossil ooze with major abundance of colorless volcanic glass, quartz & feldspar	LO *Calcidiscus macintyrei* (16.38 mbsf, 1.59 Ma)	Jiang and Wise (2007)	Berggren et al. (1995a)
1256B	3H-6	09–10	23.19	2.71	6.1	Clayey nannofossil ooze			
1256B	3H-7	23–24	24.83	2.98	6.1	Clayey nannofossil ooze			
1256B	4H-1	67–68	25.77	3.13	6.1	Sandy silty clay			
1256B	4H-2	75–76	27.35	3.39	6.1	Sandy silty clay			
1256B	4H-3	83–84	28.93	3.65	6.1	Sandy silty clay			
1256B	4H-4	90–92	30.50	3.90	6.1	Sandy silty clay			
1256B	4H-5	72–73	31.82	4.12	6.1	Sandy silty clay			
1256B	4H-7	24–25	34.34	4.53	6.1	Sandy silty clay			
1256B	5H-1	124–126	35.84	4.78	6.1	Sandy silty nannofossil ooze			
1256B	5H-6	92–94	43.02	5.67	13.2	Nannofossil ooze with diatoms	LO *Discoaster quinqueramus* (42.13 mbsf, 5.60 Ma)	Jiang and Wise (2007)	Berggren et al. (1995b)
1256B	6H-3	59–61	47.69	6.02	13.2	Nannofossil ooze with diatoms			
1256B	7H-3	54–56	57.14	6.74	13.2	Diatom nannofossil ooze			
1256B	8H-2	66–68	65.26	7.35	13.2	Nannofossil ooze with diatoms			
1256B	8H-5	89–91	66.99	7.48	13.2	Nannofossil ooze with diatoms			
1256B	9H-2	79–81	74.89	7.89	8.4	Clayey nannofossil ooze with silt	FO *Discoaster berggrenii* (80.88 mbsf, 8.60 Ma)	Jiang and Wise (2007)	Berggren et al. (1995b)
1256B	10H-4	95–97	87.55	9.39	8.4	Sandy silty nannofossil diatom ooze			
1256B	12H-5	51–53	107.61	10.88	39.1	Nannofossil ooze	LO *Sphenolithus heteromorphus* (213.78 mbsf, 13.60 Ma)	Jiang and Wise (2007)	Berggren et al. (1995b)
1256B	14H-4	79–81	125.39	11.34	39.1	Nannofossil ooze			
1256B	15H-3	37–39	132.97	11.53	39.1	Nannofossil ooze			
1256B	16H-3	132–134	143.42	11.80	39.1	Clayey nannofossil ooze			
1256B	17H-3	111–113	152.71	12.04	39.1	Nannofossil ooze			
1256B	19X-2	53–55	162.13	12.28	39.1	Nannofossil ooze with diatoms and silty clay			
1256B	20X-5	101–103	172.21	12.54	39.1	Clayey nannofossil ooze with silt			
1256B	21X-2	95–97	177.25	12.67	39.1	Nannofossil ooze with diatoms			
1256B	22X-2	45–47	185.95	12.89	39.1	Nannofossil ooze			
1256B	24X-3	79–81	207.19	13.43	39.1	Nannofossil ooze			
1256B	26X-1	89–91	223.59	13.85	39.1	Nannofossil ooze			
1256B	28X-2	54–56	243.64	14.36	39.1	Nannofossil ooze			

(*continued on next page*)

Table 1 (*continued*)

Site/hole	Core/section	Interval (cm)	Depth (mbsf)	Biostrati-graphic age estimate (Ma)	Appropriate linear sedimentation rate (m/Ma)[*]	Lithology[†]	Appropriate biohorizon, with mean depth and age, used for calculation of biostratigraphic ages	Reference for microfossil species	Reference for microfossil datum level
495	3R-5	76–77	25.76	1.11	37	Diatomaceous hemipelagic mud	LO *Discoaster brouweri* (57.0 mbsf, 1.95 Ma)	von Huene et al. (1982)	Berggren et al. (1995a)
495	6R-4	34–35	52.34	1.82	37	Biogenic silty mud			
495	9R-5	40–41	82.40	3.83	20	Diatomaceous silty mud	FO *Ceratolithus acutus* (112.60 mbsf, 5.34 Ma)	von Huene et al. (1982)	Berggren et al. (1995a)
495	12R-5	63–64	111.13	5.27	20	Siliceous mud			
495	15R-6	102–103	141.52	8.44	7	Diatomaceous mud	FO *Globorotalia plesiotumida* (142.50 mbsf, 8.58 Ma)	von Huene et al. (1982)	Lourens et al. (2004)
495	18R-7	61–62	171.11	10.77	11	Siliceous mud	LO *Discoaster kugleri* (179.10 mbsf, 11.50 Ma)	von Huene et al. (1982)	Berggren et al. (1995b)
495	21R-7	29–30	199.29	13.34	11	Nannofossil ooze			
495	24R-7	20–21	227.70	16.89	27	Nannofossil-foraminiferal ooze	LO *'Paragloborotalia' kugleri* (342.0 mbsf, 21.12 Ma)	von Huene et al. (1982)	Lourens et al. (2004)
495	27R-5	115–118	254.15	17.87	27	Nannofossil ooze			
495	30R-2	41–42	277.41	18.73	27	Foraminiferal-nannofossil ooze and chalk			
495	33R-5	41–42	310.41	19.95	27	Nannofossil ooze			
495	36R-4	50–51	337.50	20.95	27	Nannofossil ooze–chalk			
495	39R-3	108–109	365.08	21.50	58	Nannofossil-foraminiferal chalk			
495	41R-6	53–54	388.03	21.91	58	Foraminiferal-nannofossil chalk			
495	43R-5	24–25	405.24	22.21	58	Foraminiferal-nannofossil chalk with dendritic manganese			
495	45R-4	25–26	422.75	22.55	58	Foraminiferal-nannofossil chalk with dendritic manganese			

[*] Reference for linear sedimentation rate: Jiang and Wise, 2007 (Site 1256); von Huene et al., 1982 (Site 495).

[†] Reference for lithology: Wilson et al., 2003 (Site 1256); von Huene et al., 1982 (Site 495).

Table 2
Pb, Th, U concentrations (in μg/g [=ppm]) and Pb (double spike) isotope analyses of studied samples including bulk sediment (measured and initial [in]), residue (res), and leachate (lea) Pb isotope ratios. Displayed age estimates are biostratigraphic ages determined from calculations involving appropriate biohorizons of microfossil species and corresponding linear sedimentation rates. Details are provided in Table 1. Distances (dist.) to the East Pacific Rise (EPR) were calculated with the software GPlates (http://www.gplates.org; version 1.1.1).

Hole/core/section, interval (cm)	Age (Ma)	EPR dist. (km)	Pb	Th	U	$^{206}Pb/^{204}Pb$	2SE	$^{207}Pb/^{204}Pb$	2SE	$^{208}Pb/^{204}Pb$	2SE	$^{206}Pb/^{204}Pb_{in}$	$^{207}Pb/^{204}Pb_{in}$	$^{208}Pb/^{204}Pb_{in}$
ODP Leg 206, Site 1256														
1256A-1H-1, 32–34	0.04	1,299.7	13.3	3.06	1.06	18.6988	0.0006	15.6097	0.0007	38.5755	0.0016	18.6988	15.6097	38.5754
1256A-1H-2, 19–21	0.16	1,289.7	15.1	3.08	0.84	18.6921	0.0007	15.6061	0.0006	38.5631	0.0012	18.6921	15.6061	38.5630
1256A-1H-2, 19-21_res	0.16	1,289.7				18.7167	0.0008	15.6080	0.0008	38.5792	0.0026			
1256A-1H-2, 19-21_lea	0.16	1,289.7				18.6609	0.0006	15.6020	0.0006	38.5281	0.0018			
1256B-1H-4, 56–58	0.44	1,265.3	13.4	2.50	0.73	18.7053	0.0005	15.6071	0.0005	38.5746	0.0024	18.7051	15.6070	38.5743
1256B-3H-2, 34–36	1.76	1,159.6	1.64	0.93	0.30	18.7083	0.0008	15.6123	0.0009	38.5407	0.0016	18.7051	15.6122	38.5374
1256B-3H-6, 09–10	2.71	1,051.5	17.5	3.26	0.92	18.7360	0.0004	15.6281	0.0004	38.6304	0.0010	18.7345	15.6280	38.6288
1256B-3H-7, 23–24	2.98	1,028.9	13.8	3.08	0.89	18.7980	0.0004	15.6276	0.0004	38.6929	0.0013	18.7961	15.6275	38.6907
1256B-3H-7, 23–24*	2.98	1,028.9				18.7980	0.0004	15.6280	0.0004	38.6938	0.0009			
1256B-4H-1, 67–68	3.13	1,015.9	17.7	3.11	0.84	18.7466	0.0005	15.6260	0.0005	38.5802	0.0011	18.7451	15.6260	38.5784
1256B-4H-2, 75–76	3.39	994.1	10.7	2.02	0.58	18.7716	0.0005	15.6249	0.0006	38.6655	0.0017	18.7697	15.6248	38.6634
1256B-4H-3, 83–84	3.65	972.3	16.1	3.03	0.76	18.7704	0.0005	15.6263	0.0004	38.6431	0.0011	18.7687	15.6262	38.6409
1256B-4H-4, 90–92	3.90	942.6	1.26	0.30	0.08	18.8065	0.0005	15.6344	0.0005	38.7033	0.0012	18.8043	15.6343	38.7004
1256B-4H-4, 90-92_res	3.90	942.6				18.7714	0.0005	15.6231	0.0004	38.6665	0.0012			
1256B-4H-4, 90-92_lea	3.90	942.6				18.7151	0.0005	15.6250	0.0005	38.6221	0.0016			
1256B-4H-5, 72–73	4.12	924.5	13.8	2.83	0.73	18.7898	0.0010	15.6243	0.0012	38.6931	0.0039	18.7876	15.6242	38.6904
1256B-4H-7, 24–25	4.53	890.1	14.1	5.64	1.87	18.7526	0.0005	15.6189	0.0005	38.5973	0.0013	18.7467	15.6186	38.5914
1256B-5H-1, 124–126	4.78	860.6	14.6	2.77	0.68	18.7812	0.0008	15.6265	0.0006	38.6992	0.0016	18.7790	15.6264	38.6964
1256B-5H-6, 92–94	5.67	787.3	10.4	2.63	1.39	18.7858	0.0007	15.6281	0.0007	38.7114	0.0022	18.7784	15.6277	38.7068
1256B-6H-3, 59–61	6.02	748.5	7.66	1.29	1.61	18.7855	0.0007	15.6247	0.0006	38.6948	0.0016	18.7732	15.6241	38.6916
1256B-7H-3, 54–56	6.74	680.2	8.43	1.89	1.01	18.7577	0.0008	15.6164	0.0009	38.6416	0.0025	18.7498	15.6161	38.6367
1256B-8H-2, 66–68	7.35	630.7	3.47	0.84	0.32	18.7645	0.0009	15.6240	0.0009	38.6122	0.0025	18.7580	15.6237	38.6064
1256B-8H-5, 89–91	7.48	620.2	6.35	1.47	0.46	18.7530	0.0007	15.6225	0.0006	38.6636	0.0016	18.7476	15.6222	38.6580
1256B-8H-5, 89–91_res	7.48	620.2				18.7688	0.0009	15.6176	0.0008	38.6629	0.0024			
1256B-8H-5, 89-91_lea	7.48	620.2				18.7308	0.0013	15.6215	0.0014	38.6616	0.0044			
1256B-9H-2, 79–81	7.89	586.0	4.24	0.86	0.30	18.7263	0.0007	15.6100	0.0007	38.5738	0.0021	18.7207	15.6098	38.5685
1256B-10H-4, 95–97	9.39	454.7	11.5	1.30	0.43	18.6743	0.0009	15.5934	0.0010	38.5275	0.0028	18.6708	15.5932	38.5239
1256B-12H-5, 51–53	10.88	330.1	3.40	0.45	1.43	18.7025	0.0007	15.5931	0.0006	38.5138	0.0014	18.6575	15.5910	38.5091
1256B-14H-4, 79–81	11.34	295.3	1.17	0.10	0.36	18.7344	0.0013	15.5965	0.0013	38.5787	0.0035	18.7002	15.5949	38.5756
1256B-15H-3, 37–39	11.53	280.5	1.93	0.16	0.25	18.6221	0.0007	15.5765	0.0006	38.4308	0.0016	18.6073	15.5758	38.4278
1256B-16H-3, 132–134	11.80	266.2	1.81	0.12	0.21	18.6440	0.0013	15.5896	0.0013	38.4846	0.0040	18.6303	15.5890	38.4820
1256B-17H-3, 111–113	12.04	247.6	1.89	0.11	0.32	18.7516	0.0009	15.5924	0.0008	38.5061	0.0020	18.7312	15.5915	38.5039
1256B-19X-2, 53–55	12.28	228.8	1.93	0.15	1.20	18.7087	0.0006	15.5900	0.0006	38.4893	0.0015	18.6334	15.5865	38.4863
1256B-20X-5, 101–103	12.54	208.6	1.05	0.08	0.48	18.6987	0.0006	15.5903	0.0005	38.5128	0.0012	18.6416	15.5877	38.5096
1256B-21X-2, 95–97	12.67	198.5	2.61	0.11	0.64	18.6382	0.0009	15.5737	0.0008	38.4190	0.0021	18.6077	15.5723	38.4172
1256B-21X-2, 95-97_res	12.67	198.5				18.6715	0.0012	15.5782	0.0011	38.4522	0.0028			
1256B-21X-2, 95-97_lea	12.67	198.5				18.6367	0.0020	15.5758	0.0019	38.4139	0.0052			
1256B-22X-2, 45–47	12.89	188.4	2.84	0.14	0.32	18.6377	0.0010	15.5743	0.0010	38.4192	0.0025	18.6235	15.5737	38.4171

(*continued on next page*)

Table 2 (*continued*)

Hole/core/section, interval (cm)	Age (Ma)	EPR dist. (km)	Pb	Th	U	$^{206}Pb/^{204}Pb$	2SE	$^{207}Pb/^{204}Pb$	2SE	$^{208}Pb/^{204}Pb$	2SE	$^{206}Pb/^{204}Pb_{in}$	$^{207}Pb/^{204}Pb_{in}$	$^{208}Pb/^{204}Pb_{in}$
1256B-24X-3, 79–81	13.43	144.1	2.05	0.09	0.17	18.5864	0.0006	15.5601	0.0006	38.3397	0.0017	18.5755	15.5596	38.3377
1256B-24X-3, 79–81*	13.43	144.1				18.5880	0.0006	15.5612	0.0007	38.3444	0.0023			
1256B-26X-1, 89-91	13.85	110.6	1.76	0.13	0.07	18.5980	0.0006	15.5601	0.0005	38.3571	0.0012	18.5930	15.5598	38.3537
1256B-28X-2, 54–56	14.36	68.5	5.22	0.21	0.09	18.6282	0.0008	15.5587	0.0007	38.3701	0.0021	18.6258	15.5585	38.3682
1256B-28X-2, 54-56_res	14.36	68.5				18.6595	0.0009	15.5654	0.0010	38.4190	0.0029			
1256B-28X-2, 54-56_lea	14.36	68.5				18.6387	0.0008	15.5630	0.0007	38.3820	0.0018			
DSDP Leg 67, Site 495†														
495-3R-5, 76–77	1.11	1,495.8	5.86	2.15	5.87	18.7543	0.0007	15.6298	0.0009	38.5514	0.0030	18.7433	15.6293	38.5501
495-6R-4, 34–35	1.82	1,412.7	8.61	2.73	7.36	18.7791	0.0010	15.6148	0.0011	38.5942	0.0036	18.7637	15.6141	38.5923
495-9R-5, 40–41	3.83	1,229.0	9.69	3.03	5.50	18.7579	0.0012	15.6173	0.0012	38.6071	0.0034	18.7363	15.6163	38.6032
495-12R-5, 63–64	5.27	1,103.2	11.2	4.30	4.46	18.7811	0.0008	15.6208	0.0008	38.6240	0.0020	18.7604	15.6198	38.6174
495-15R-6, 102–103	8.44	846.5	9.76	2.51	4.18	18.7414	0.0008	15.6080	0.0010	38.5599	0.0030	18.7056	15.6064	38.5528
495-18R-7, 61–62	10.77	674.1	12.4	3.25	1.97	18.6509	0.0009	15.5778	0.0011	38.4180	0.0035	18.6339	15.5770	38.4087
495-21R-7, 29–30	13.34	514.6	3.26	0.22	0.16	18.5488	0.0008	15.5501	0.0009	38.2642	0.0028	18.5422	15.5498	38.2613
495-24R-7, 20–21	16.89	349.4	5.85	0.38	0.16	18.4400	0.0009	15.5360	0.0010	38.1426	0.0035	18.4355	15.5358	38.1390
495-27R-5, 115–118	17.87	299.2	6.13	0.44	0.13	18.5049	0.0007	15.5553	0.0009	38.2371	0.0027	18.5013	15.5551	38.2330
495-30R-2, 41–42	18.73	246.8	4.47	0.25	0.10	18.4271	0.0008	15.5331	0.0007	38.1200	0.0022	18.4230	15.5330	38.1167
495-33R-5, 41–42	19.95	171.3	1.55	0.08	0.13	18.4545	0.0005	15.5304	0.0004	38.1265	0.0012	18.4387	15.5297	38.1232
495-36R-4, 50–51	20.95	100.4	1.45	0.06	0.13	18.5428	0.0010	15.5546	0.0011	38.2559	0.0036	18.5239	15.5537	38.2529
495-39R-3, 108–109	21.50	67.0	7.57	0.01	0.08	18.4515	0.0007	15.5297	0.0009	38.1335	0.0028	18.4493	15.5296	38.1334
495-41R-6, 53–54	21.91	41.8	1.13	0.09	0.20	18.4471	0.0006	15.5276	0.0005	38.1146	0.0016	18.4097	15.5259	38.1090
495-41R-6, 53–54*	21.91	41.8				18.4493	0.0005	15.5284	0.0004	38.1175	0.0010			
495-43R-5, 24–25	22.21	23.7	2.20	0.09	0.08	18.4041	0.0008	15.5233	0.0008	38.0693	0.0025	18.3964	15.5230	38.0662
495-45R-4, 25–26	22.55	5.3	8.32	0.19	0.36	18.2899	0.0008	15.5057	0.0010	37.9331	0.0035	18.2803	15.5053	37.9315

Sample numbers with * are replicate analyses on separate sample dissolutions.

2SE = twofold standard error. The long-term average Pb–DS corrected NBS981 values and associated 2SDs have been $^{206}Pb/^{204}Pb = 16.9420 \pm 0.0030$, $^{207}Pb/^{204}Pb = 15.4998 \pm 0.0029$, $^{208}Pb/^{204}Pb = 36.7256 \pm 0.0072$, $^{207}Pb/^{206}Pb = 0.91487 \pm 0.00006$, $^{208}Pb/^{206}Pb = 2.16772 \pm 0.00010$ ($n = 139$). These NBS981 values agree well with other double- and triple-spike data for NBS981 (Galer, 1999; Thirlwall, 2000, 2002; Baker et al., 2004, 2005).

† Pb, Th, U concentrations of DSDP Site 495 are taken from Patino et al. (2000).

mass bias correction. The DS values for the MAT262 RPQ^{2+} TIMS are $^{204}Pb/^{206}Pb = 9.24856$, $^{207}Pb/^{206}Pb = 36.7129$, and $^{208}Pb/^{206}Pb = 1.86007$. Following the heat-up procedure of Kuritani and Nakamura (2002), measurements were usually carried out at 3–5 V beam intensities on ^{208}Pb (common Pb) and ^{207}Pb (spiked Pb). In general, beam stability was ±20% over the course of 3–5 data blocks (20 integrations each block), which added up to 15–25 min for each acquisition. Pb–DS reduction followed the algorithms delineated by Johnson and Beard (1999, and references therein). Over the course of the project (2006–2012), the long-term average Pb–DS corrected NBS981 values and associated 2SDs have been $^{206}Pb/^{204}Pb = 16.9420 \pm 0.0030$, $^{207}Pb/^{204}Pb = 15.4998 \pm 0.0029$, $^{208}Pb/^{204}Pb = 36.7256 \pm 0.0072$, $^{207}Pb/^{206}Pb = 0.91487 \pm 0.00006$, $^{208}Pb/^{206}Pb = 2.16772 \pm 0.00010$ ($n = 139$). These NBS981 values agree well with other double- and triple-spike data for NBS981 (Galer, 1999; Thirlwall, 2000, 2002; Baker et al., 2004, 2005). Duplicate analyses of samples 206-1256B-3H-7, 23–24 cm, 206-1256B-24X-3, 79–81 cm, and 67–495-41R-6, 53–54 cm were identical within 2SD of NBS981 (Table 2). Total procedural Pb blanks obtained for sample dissolution and chromatography ranged from 6 to 20 pg, except one 75 pg outlier. This blank level is considered negligible compared to the total amount of sample Pb extracted.

Initial Pb isotope ratios of bulk sediments were calculated using the algorithms outlined in Faure and Mensing (2005). The required Pb, Th, and U concentrations of Site 1256 sediments were obtained by inductively coupled plasma mass spectrometry (ICP-MS) on a ThermoFinnigan Element2 at the Department of Geosciences, University of Bremen. Sample digest and analyte solutions were prepared following the procedures outlined in Geldmacher et al. (2008). Pb, Th, and U concentrations for Site 495 sediments are from Patino et al. (2000).

4. RESULTS

Measured Pb isotopic compositions of the bulk sediments of Site 495 ($^{206}Pb/^{204}Pb = 18.29–18.78$; $^{207}Pb/^{204}Pb = 15.51–15.63$; $^{208}Pb/^{204}Pb = 37.93–38.62$) are on average somewhat less radiogenic than those of Site 1256 ($^{206}Pb/^{204}Pb = 18.59–18.81$; $^{207}Pb/^{204}Pb = 15.56–15.63$; $^{208}Pb/^{204}Pb = 38.34–38.71$; Table 2), but generally the data from the two cores overlap and form a consistent time series (Fig. 4) despite significant changes in sediment facies at each site over time. The bulk sediment Pb isotopic compositions increased continuously from ~22.5 Ma at Site 495 and from ~13.4 Ma at Site 1256 to maximum values of $^{206}Pb/^{204}Pb$ and $^{207}Pb/^{204}Pb$ at ~4 Ma, while $^{208}Pb/^{204}Pb$ reached maximum values between ~6 and 4 Ma (Fig. 4). Since ~4–3 Ma, the Pb isotope ratios have then become systematically less radiogenic (Fig. 4). At ~1.8 Ma, they reached eastern equatorial Pacific seawater values (Fig. 4), as recorded by a Fe–Mn crust (GMAT 14D; Frank et al., 1999) from the northern Cocos Plate seafloor located at a distance of ~1100 km (Site 495) and ~2000 km (Site 1256), respectively (Fig. 1a). Although being slightly offset to less radiogenic values prior to ~1.8 Ma, the seawater Pb isotopic evolution recorded by this Fe–Mn crust over the past ~7 million years shows a variability very similar to our bulk Pb isotopic compositions (Fig. 4), as expected from the very short mean oceanic residence time of Pb. The residence time of Pb is considered to be particularly low in the study area (~5–10 years), since particle fluxes are high (Henderson and Maier-Reimer, 2002).

While there is a broad overlap of the Site 1256 and 495 data sets at any given point of time, this does not apply when taking into consideration the increasing distance of each site to the East Pacific Rise (EPR) with increasing age as a result of Cocos Plate motion. Given the same distance to the EPR, the Pb isotopic composition at Site 495 is significantly less radiogenic than at Site 1256 for distances below ~1000 km (Fig. 5). At distances exceeding 1000 km, the Pb isotopic composition at both sites became similar (Fig. 5).

The Pb isotopic compositions obtained from both residues (reflecting detrital input) and leachates (reflecting past ambient seawater) of five samples of Site 1256 closely follow the temporal evolution recorded by the bulk sediments (Fig. 4), which supports common controlling factors. While

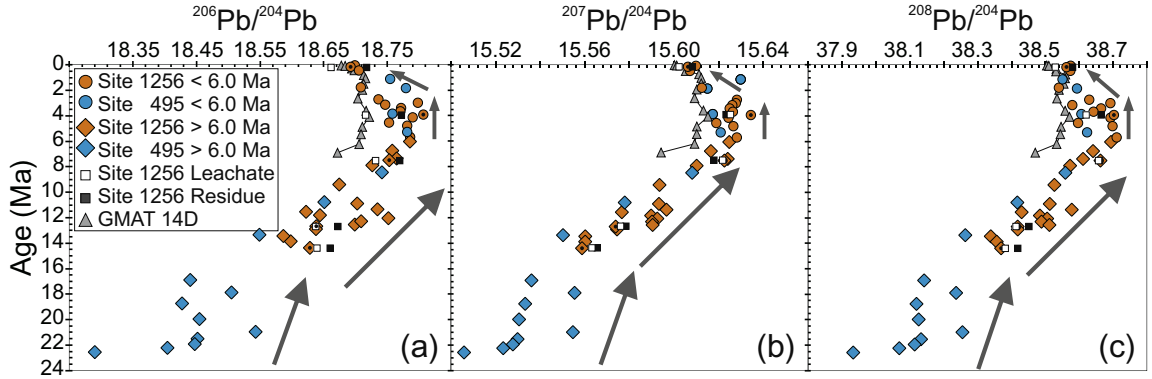

Fig. 4. Sites 495/1256 $^{206}Pb/^{204}Pb$ (a), $^{207}Pb/^{204}Pb$ (b), and $^{208}Pb/^{204}Pb$ (c) isotope ratios versus age (Ma). Data from eastern equatorial Pacific Fe–Mn crust GMAT 14D (Frank et al., 1999) are also shown for comparison. Black dots placed on distinct orange symbols refer to those Site 1256 samples from which the coeval leachate (white squares) and residual data (black squares) were obtained. Errors are within symbol sizes. (For interpretation of the references to color in this figure legend, the reader is referred to the web version of this article.)

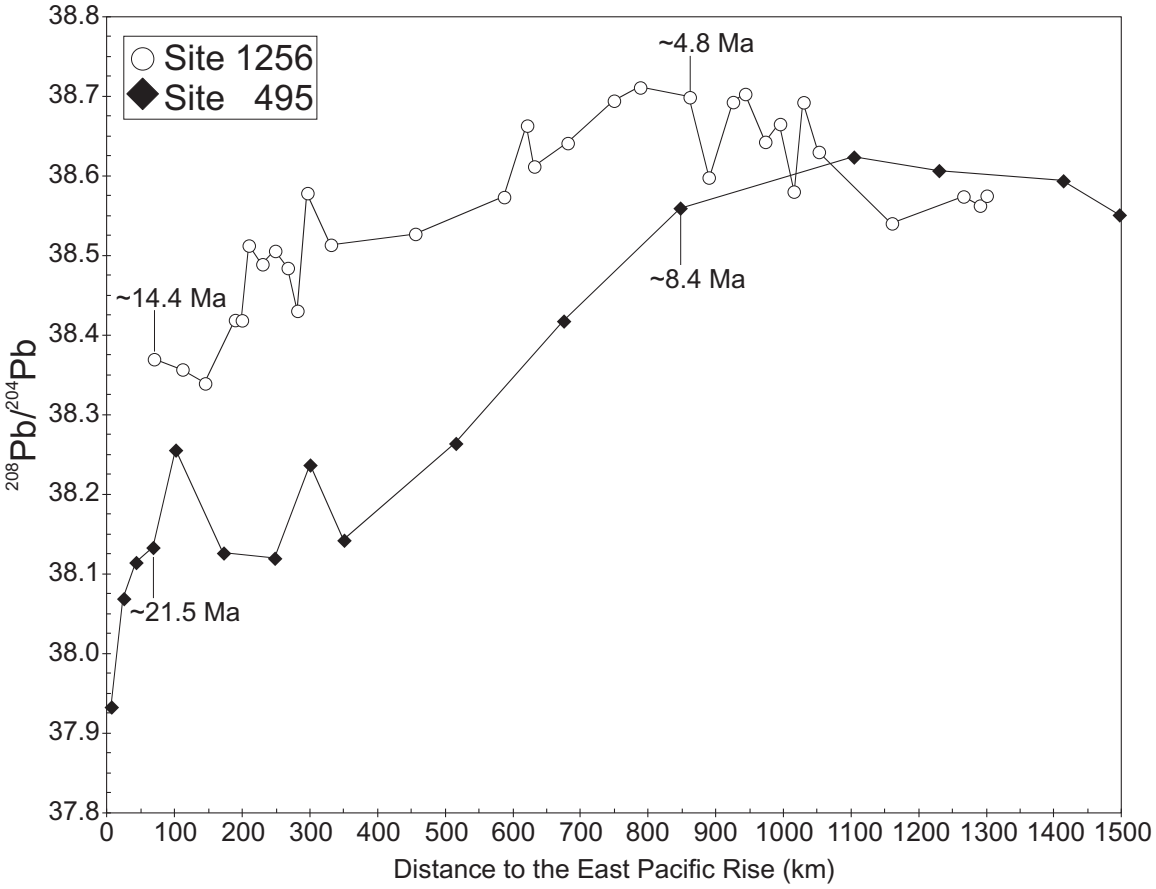

Fig. 5. Sites 495 and 1256 $^{208}Pb/^{204}Pb$ isotope ratio versus distance of each site to the East Pacific Rise in kilometer (km) over time. Distances to the East Pacific Rise were calculated with the software GPlates (http://www.gplates.org; version 1.1.1). Additionally, they are provided in Table 2.

$^{207}Pb/^{204}Pb$ generally showed no significant differences between leachate and residue, the $^{206}Pb/^{204}Pb$ and $^{208}Pb/^{204}Pb$ signatures of the residues were more radiogenic than the seawater-derived leachate compositions. For the samples older than ~6 Ma, whose composition was dominated by biogenic oozes (Wilson et al., 2003), the residues also generally had more radiogenic Pb isotopic compositions than the bulk sediments (Fig. 4). For the sediments younger than 6 Ma dominated by terrigenous material (Wilson et al., 2003), the Pb isotopic compositions of the residues were less radiogenic or identical to those of the bulk sediments. After 6 Ma, the seawater (leachate) Pb isotopic signal obtained from Site 1256 was similar to that of Fe–Mn crust GMAT 14D, whereas prior to 6 Ma one sediment leachate data point was somewhat more radiogenic. Within the older nannofossil ooze sequence, the leachate data are commonly identical to the bulk compositions or slightly shifted to more radiogenic Pb isotope ratios (Fig. 4). This may reflect minor partial dissolution of detrital particles during the leaching procedure for the Fe–Mn coatings, leading to small shifts of the Pb isotopic composition toward that of the detrital fraction, similar to observations of Wilson et al. (2015). In addition, one sample from the clastic-dominated upper part of the sediment core (1256B-4H-4, 90–92) revealed bulk Pb isotopic compositions more radiogenic than both residue and leachate fraction. A less radiogenic residue composition may be the result of incomplete decarbonation giving rise to somewhat less radiogenic detrital compositions. The fact that the leachate data also show less radiogenic Pb isotope ratios most likely reflects heterogeneities of the bulk sample, implying that the bulk sample material used for the leaching experiment had a less radiogenic Pb isotopic composition than the corresponding bulk sample from this same core section (see Section 3). A somewhat higher heterogeneity of the bulk sediment composition can also be seen through the larger variability of Pb isotope ratios of clastic-rich samples of nearly the same age younger than ~3.5–2.5 Ma (Fig. 4). It is noted that the effects described above did not affect the general temporal Pb isotopic evolution observed.

5. DISCUSSION

5.1. Identification of source end-members of eastern equatorial Pacific sediments

Seafloor sediments record the radiogenic isotopic signal of the source area from which they are derived and we thus compare our measured sedimentary Pb isotope data with

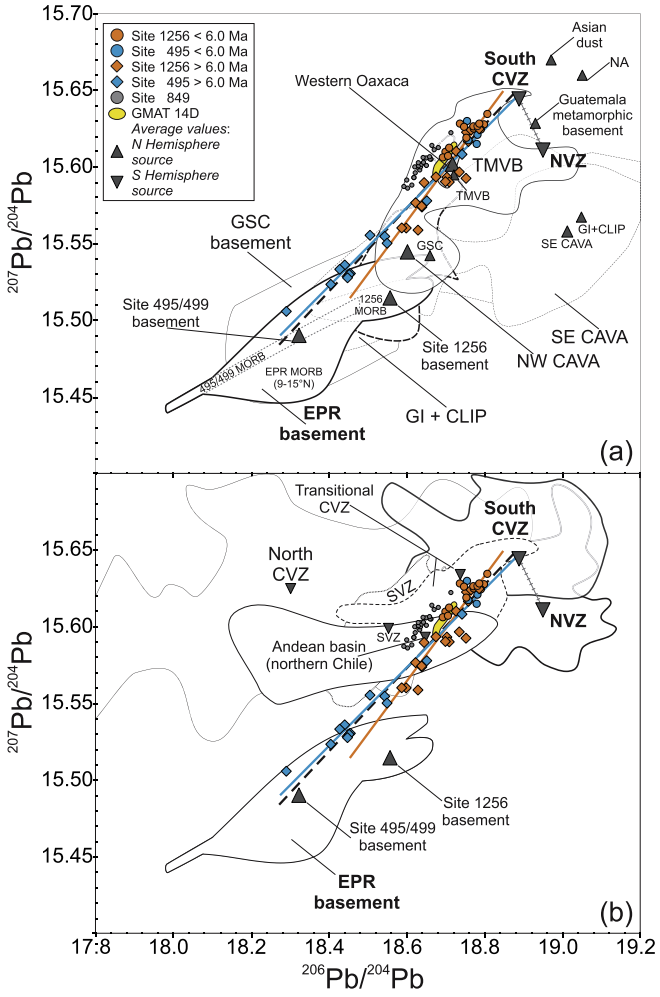

Fig. 6. $^{206}Pb/^{204}Pb$ versus $^{207}Pb/^{204}Pb$ for constraining potential (a) Northern Hemisphere and (b) Southern Hemisphere sediment sources, respectively. The presented Pb isotope data constitute a narrowly defined sediment array ($R^2 = 0.94$ for both sites combined, associated with the corresponding dashed black regression line), reflected by highly linear correlations (1256 (orange regression line): $R^2 = 0.85$, 495 (blue regression line): $R^2 = 0.97$). The isotopic arrays reveal linear two-component mixing between East Pacific Rise (EPR) mid-ocean ridge basalt (MORB) and active continental margins of Mexico (igneous complexes of southern Mexico ± Trans-Mexican Volcanic Belt) and western South America (South Central Volcanic Zone and Northern Volcanic Zone). Shown mixing line between the South CVZ and the NVZ (dark gray) is marked by small ticks representing 10% increments. Regular and upside-down triangles depict average compositions of Northern and Southern Hemisphere geological units, respectively. Abbreviations are the same as in Fig. 1a/b. Errors are smaller than symbol sizes. Data sources: GMAT 14D (Frank et al., 1999); MORB (mid-ocean-ridge basalt) from Site 1256 (Geldmacher et al., 2013), Sites 495/499 (Geldmacher et al., 2008, 2013; Heydolph et al., 2012) (fields for both sites based on initial isotope data) and EPR (9–15°N) (Castillo et al., 2000; Sims et al., 2002; Goss et al., 2010; Waters et al., 2011); western Oaxaca (Martiny et al., 2000); central Andean forearc basin (Lucassen et al., 2002); Asian dust end-member (Pettke et al., 2000); North American (NA) end-member (Stancin et al., 2006). All other data fields and/or calculated average compositions (CAVA, CLIP (uplifted fragments of the Pacific part), GI (including Cocos Island and associated seamounts), GSC, Guatemala metamorphic basement (part of Chortís Block), NVZ, North/Transitional/South CVZ, SVZ, and TMVB), respectively, are based on Pb isotope data from either the GEOROC database (http://georoc.mpch-mainz.gwdg.de/georoc/) or the PetDB database (http://www.earthchem.org/petdb) retrieved in November/December 2015 and provided in the electronic appendix (Table A.1). See electronic appendix Section A.1 for criteria of Pb isotopic database construction. (For interpretation of the references to color in this figure legend, the reader is referred to the web version of this article.)

literature data of the potential source areas (Table 2 demonstrates that radiogenic ingrowth of the sedimentary Pb isotopic compositions is insignificant for the studied time interval). The identification of specific source contributions from bulk sediment data in the case of Pb isotopes needs to take into account that the bulk sediment record is influenced by multiple parameters including source origin, different sedimentary phases, and transport processes.

The Pb isotope data for both studied sites correlate well on Pb–Pb isotope diagrams: $R^2 = 0.94$ for both sites combined and $R^2 = 0.85$ (1256) and $R^2 = 0.97$ (495) separately on the $^{206}Pb/^{204}Pb$ versus $^{207}Pb/^{204}Pb$ as well as $R^2 = 0.97$ combined and $R^2 = 0.90$ (1256) and $R^2 = 0.99$ (495) on the $^{206}Pb/^{204}Pb$ versus $^{208}Pb/^{204}Pb$ isotope diagrams (Figs. 6 and 7). The pronounced linear correlations on the Pb isotope diagrams suggest mixing of a relatively depleted

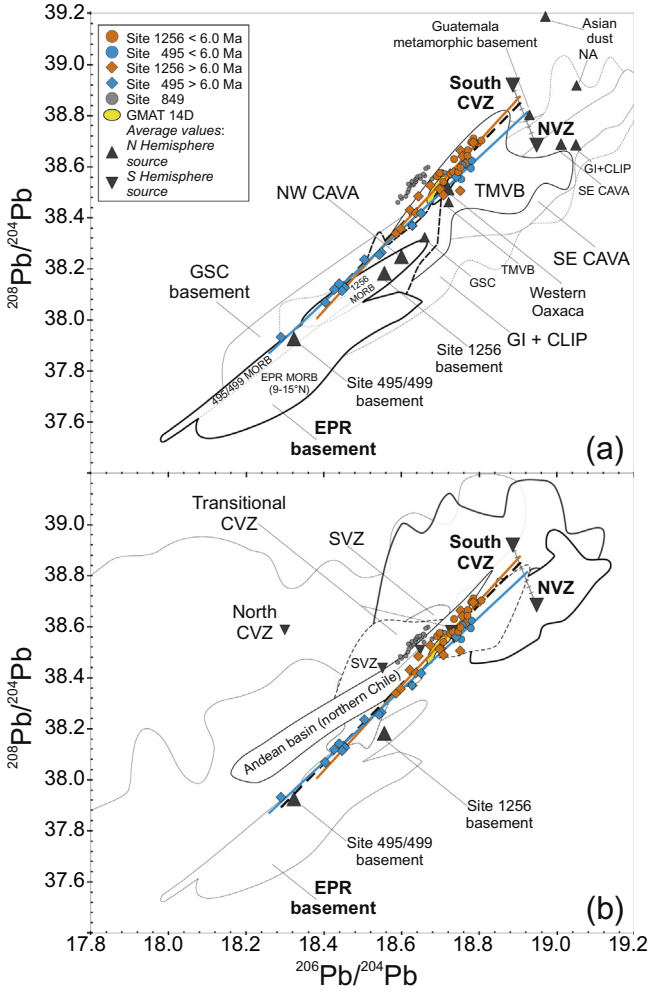

Fig. 7. $^{206}Pb/^{204}Pb$ versus $^{208}Pb/^{204}Pb$ for constraining potential (a) Northern Hemisphere and (b) Southern Hemisphere sediment sources, respectively. The presented Pb isotope data constitute a narrowly defined sediment array ($R^2 = 0.97$ for both sites combined, associated with the corresponding dashed black regression line), reflected by highly linear correlations (1256 (orange regression line): $R^2 = 0.90$, 495 (blue regression line): $R^2 = 0.99$). The isotopic arrays reveal linear two-component mixing between East Pacific Rise (EPR) mid-ocean ridge basalt (MORB) and active continental margins of Mexico (igneous complexes of southern Mexico ± Trans-Mexican Volcanic Belt) and western South America (South Central Volcanic Zone and Northern Volcanic Zone). Shown mixing line between the South CVZ and the NVZ (dark gray) is marked by small ticks representing 10% increments. Regular and upside-down triangles depict average compositions of Northern and Southern Hemisphere geological units, respectively. Abbreviations are the same as in Fig. 1a/b. Errors are smaller than symbol sizes. Data sources are the same as for Fig. 6. See electronic appendix Section A.1 for criteria of Pb isotopic database construction. (For interpretation of the references to color in this figure legend, the reader is referred to the web version of this article.)

component with unradiogenic Pb and an enriched component with radiogenic Pb isotopic composition throughout the entire period. The data of Fe–Mn crust GMAT 14D plots on the arrays formed by Sites 495 and 1256 bulk sediments (Figs. 6 and 7) suggesting that the same two end-members have controlled the seawater Pb isotopic composition recorded by that Fe–Mn crust.

5.1.1. The unradiogenic component

When constraining the unradiogenic source components, the igneous basement formed at the Galápagos Spreading Center (GSC) is, on average, significantly offset from the sediment arrays on the uranogenic Pb isotope diagram (Fig. 6a) and thus cannot serve as the unradiogenic end-member. In contrast, the Cocos Plate mid-ocean ridge basalt (MORB) basement formed at the East Pacific Rise (EPR) has the appropriate composition to serve as the unradiogenic end-member of the two-component mixing lines for both studied sites. The slopes of the regression lines for the two sites, however, differ in that Site 1256 shows a slightly steeper slope compared to Site 495, particularly on the uranogenic diagram (Fig. 6). An extension of the Site 1256 array (best-fit line) intersects the field of Site 1256 MORB basement, whereas the Site 495 array projects into Site 495/499 MORB crust (Figs. 6a and 7a). The difference in the basement composition of the two sites is also reflected in the more enriched Pb isotopic composition of the basal sediments at Site 1256 (Fig. 4). This initial compositional

difference appears to have exerted an influence on the isotopic evolution at both studied sites, as indicated by consistently higher Pb isotope ratios at Site 1256 compared to Site 495 at a given distance from the EPR (Fig. 5). Only at distances >900 km from the EPR, the influence of the different basement compositions disappears (Fig. 5).

The difference in Pb isotopic composition of the depleted MORB source end-members most likely reflects the varying impact of the Galápagos Hotspot on the EPR during the Miocene. Geldmacher et al. (2013) have shown that influx of Galápagos plume material into the EPR took place from ~22.5–11 Ma during superfast spreading along the EPR between ~3°S and ~5°N and reached a maximum between 18 and 15 Ma. This is consistent with more enriched, Galápagos-like Pb isotopic compositions of the crust of Site 1256, which formed at 15.2 Ma, than that of Site 495, the basement of which formed prior to the major influx of Galápagos plume material. In addition, the basement of Site 495 was produced further north (Fig. 1a) and thus less Galápagos plume material likely reached the EPR where Site 495 basement was formed. Since only high-temperature fluids can leach major amounts of Pb from MORB oceanic crust, hydrothermal activity at the spreading center is an important mechanism for transferring dissolved and particulate Pb with MORB composition into the water column (e.g., Chen et al., 1986; Barrett et al., 1987). We therefore propose that hydrothermal activity at the EPR was the ultimate source of the depleted end-member in the sedimentary successions (see Section 5.2.1 for discussion of the transport pathway) and that hydrothermal particulate Pb from the EPR contributed to the Pb isotopic budget of the sediments over their entire ~23 Ma history.

5.1.2. The radiogenic component: Constraining Northern Hemisphere dust sources

Identification of the isotopically enriched component of the sedimentary Pb isotopic arrays is more challenging (see Section A.1 and Table A.1 of the electronic appendix for databases of potential terrigenous sources). Various source areas from the Northern and Southern Hemispheres have to be taken into consideration as potential radiogenic end-members (Fig. 1). In the Northern Hemisphere, volcanic debris may have been derived from either (1) continental magmatic suites of southern Mexico, (2) oceanic igneous complexes related to the Galápagos Hotspot (Galápagos Islands, including Cocos Island and associated hotspot tracks, older Galápagos Hotspot terranes accreted to the Costa Rica and Panamanian margin, and uplifted portions of the Caribbean Large Igneous Province), and/or (3) continental arcs, i.e., the Trans-Mexican Volcanic Belt and the Central American Volcanic Arc (Fig. 1a). Moreover, non-volcanic detritus may have been transported from both the proximal continental basement of northern Central America and the distal North American and central Asian continental sources. The Andean Arc, forming the western active continental margin of South America, may also have provided major amounts of material to the study area (Fig. 1b; see Section 5.1.3).

The influence of explosive volcanism on the Pb isotope record is considered to be minor to negligible for the present study, since sampling of discrete tephra layers was avoided and disseminated tephra particles are only present in minor to trace amounts (von Huene et al., 1982; Wilson et al., 2003), accounting for, e.g., at maximum ~1–2 vol% of the terrigenous material at Site 1256 (Wilson et al., 2003). Thus, contributions of volcanic arc material to the studied sediments would have to be supplied through erosion and subsequent transport of the detrital material.

We first consider proximal igneous crustal units, such as the Galápagos Archipelago, as potential radiogenic sediment sources. Although the age of the present archipelago is younger than 4 Ma, it has been shown that its submarine (now drowned) tracks (Cocos, Coiba, and Carnegie Ridges) continuously formed ancient Galápagos Archipelagoes at the location of the present islands over the past ~20 Myr (Werner et al., 1999; Werner and Hoernle, 2003). Older (~70–20 Ma) portions of the hotspot tracks were accreted to the Pacific margin of Panama and Costa Rica and probably have been subaerially exposed since the Late Cretaceous (Hauff et al., 2000; Hoernle et al., 2002). Uplifted portions of the margin of the Caribbean Large Igneous Province (CLIP) are also exposed along the coasts of southern Central America and Colombia (Hauff et al., 1997, 2000; Kerr et al., 1997; Hoernle et al., 2002). The nearby Central American Volcanic Arc (CAVA) has been active throughout the history of sedimentation at Sites 495 and 1256. Since the Early Miocene, the CAVA volcanism has undergone three different stages of intense arc magmatism (Middle Miocene, Late Miocene to Pliocene, Late Quaternary; Alvarado et al., 2007, and references therein). The CAVA can be subdivided into an isotopically distinct northwestern (NW) part including Guatemala, El Salvador, Honduras and NW Nicaragua (Heydolph et al., 2012) and a southeastern (SE) part including southwestern Nicaragua, Costa Rica, and Panama (Feigenson et al., 2004; Hoernle et al., 2008; Gazel et al., 2009, 2011). Located more distal compared to the CAVA, i.e., between 18°N and 21.5°N (Fig. 1a), the formation of the Trans-Mexican Volcanic Belt (TMVB) began at ~20 Ma upon Upper Cretaceous to Oligocene subduction-related igneous complexes that are, in turn, underlain by a Precambrian to Mesozoic terrane assemblage (Ferrari et al., 2012, and references therein). The area to the south of the TMVB toward the Pacific coast is marked by a pre-Neogene arc with transtensional tectonic features, forming two igneous provinces referred to as inland volcanic sequences (IVS) and coastal plutonic belt (CPB), respectively (Morán-Zenteno et al., 1999; Martiny et al., 2000; Fig. 1a). They are Oligocene in age and underlain by a pre-Cenozoic metamorphic basement principally made up of three terranes termed Mixteca, Oaxaca, and Xolapa (Martiny et al., 2000).

The Northern Hemisphere volcanic complexes of the CLIP or SE CAVA in southeastern Central America or of the Galápagos Islands (GI) nearest to our study sites cannot, however, serve as the radiogenic end-member because their Pb isotopic compositions overall lie significantly below the mixing lines defined by the bulk sediments of the two cores (Figs. 6a and 7a). The continental basement most proximal to the studied drill sites is represented by the locally exposed Guatemala metamorphic basement

as part of the Chortís Block, which extends from Guatemala to northeastern Nicaragua (e.g., Feigenson et al., 2004; Rogers et al., 2007; Heydolph et al., 2012). However, these rocks cannot serve as the radiogenic Pb end-member either, since their average $^{207}Pb/^{204}Pb$ and $^{208}Pb/^{204}Pb$ are also too low for a given $^{206}Pb/^{204}Pb$ (Figs. 6a and 7a). Therefore, the geological units geographically closest to the studied sites of sedimentation are not suitable end-members. Although NW CAVA samples have Pb isotopic compositions closer to the sediment mixing lines of both studied sites, the NW CAVA Pb isotope data alone are also too unradiogenic on average to serve as the only enriched end-member (Figs. 6a and 7a). This holds true for the more distal arc-related complexes of central (TMVB) and southern (IVS, CPB) Mexico as well (Figs. 6a and 7a).

Since the most proximal sources do not have appropriate Pb isotopic compositions to serve as the enriched end-member, we will now consider more distal (dust) sources in the Northern Hemisphere. The eastern Pacific ITCZ represents a marked barrier for Northern Hemisphere dust, particularly from central Asia (e.g., Rea, 1994; Jones et al., 2000; Pettke et al., 2000, 2002; Stancin et al., 2006), where desertification commenced by 22 Ma based on loess studies in north central China (Guo et al., 2002). Nevertheless, the studied drill sites may have been affected by the most distal Northern Hemisphere continental dust sources of Asia and North America during their younger histories due to their northward migration and crossing of the ITCZ between ~6 Ma at Site 495 and ~4–3 Ma at Site 1256 (Fig. 2b), after which they have been subjected to the atmospheric circulation of the Northern Hemisphere. Both the highly radiogenic average Pb isotopic compositions of central Asian dust (Pettke et al., 2000) and of western North American hemipelagic clay (Stancin et al., 2006), however, deviate overall significantly from the extrapolation of the sediment arrays on the Pb isotope variation diagrams (Figs. 6a and 7a). Thus, they cannot represent the sole radiogenic end-member(s) either. The main argument against a significant impact of these two source areas, however, comes from the temporal trend of the sedimentary Pb isotope record, showing a peak at ~6–4 Ma and decreasing values thereafter (Fig. 4). The opposite pattern would be expected north of the ITCZ in view of the highly radiogenic composition of both distant continental Northern Hemisphere sources.

5.1.3. The radiogenic component: Constraining Southern Hemisphere dust sources

Having shown that Northern Hemisphere sources cannot serve as the radiogenic end-member, we now evaluate distal sources from the Southern Hemisphere. The Andean Arc has been active since the Lower Jurassic and forms the western continental margin of South America. It has been grouped into four volcanic domains, referred to as Northern Volcanic Zone (NVZ: 5°N–2°S), Central Volcanic Zone (CVZ: 14.5°–27.5°S), Southern Volcanic Zone (SVZ: 33°–46°S), and Austral Volcanic Zone (AVZ: 49°–55°S) (reviewed by Stern, 2004). Applying the literature-based compositional subdivision of the CVZ (Faure, 2001, and references therein) used by Pichat et al. (2014), we have additionally subdivided the CVZ into three parts, termed the North (14.5°–19.5°S), Transitional (20.5°–21.5°S), and South CVZ (22°–27.5°S) (Fig. 1b). In contrast to the volcanic arc, Pb isotope data from fore- and rear-arc Andean basins are scarce. For this study, we also consider the Andean forearc in the arid southern Central Andes on the Pacific coast of northern Chile (Fig. 1b), which comprises mafic to intermediate igneous rocks emplaced during the Jurassic and Lower Cretaceous (Lucassen et al., 2002, and references therein). Comparing the distribution of data of ancient and recent samples in the Pb isotope variation diagrams, no igneous unit considered shows major changes in Pb isotopic composition through time (see Table A.1 of the electronic appendix).

The Andean Arc can serve as a potential radiogenic end-member, since the studied sites were located south of the ITCZ until ~6–4 Ma ago (Fig. 2a/b). A complex pattern results from plotting the data fields and average values of the Andean Arc segments (NVZ; North, Transitional, and South CVZ; and SVZ) in Pb–Pb isotopic space (Figs. 6b and 7b). The NVZ, the most proximal Andean arc segment to the studied drill sites, cannot alone serve as the radiogenic end-member, since its $^{207}Pb/^{204}Pb$ and $^{208}Pb/^{204}Pb$ ratios are overall too low for a given $^{206}Pb/^{204}Pb$ ratio (Figs. 6b and 7b). The three segments of the more southerly CVZ display considerable variability in Pb isotopic compositions, but the North CVZ segment is far too unradiogenic in its average $^{206}Pb/^{204}Pb$ isotopic signature to serve as the enriched end-member (Fig. 6b). The Transitional CVZ segment does not fit either, since its average $^{206}Pb/^{204}Pb$ and $^{208}Pb/^{204}Pb$ signatures are too unradiogenic and the average $^{207}Pb/^{204}Pb$ isotope ratio is considerably more radiogenic than that of the sediments (Figs. 6b and 7b). The South CVZ segment, on the other hand, covers a substantial part of the sediment record and its average Pb isotopic composition is close to the radiogenic end of the combined Site 495 and Site 1256 sediment array on the uranogenic Pb isotope variation diagram (Fig. 6b). Nonetheless, the average composition plots slightly above the sediment arrays (for each site and combined) on the thorogenic Pb plot (Fig. 7b). Thus, the South CVZ is most likely not the exclusive radiogenic end-member. The Andean forearc area of arid coastal northern Chile is also part of the South CVZ segment, but based on the Pb isotope data from an arc-related Mesozoic igneous complex exposed in the northern Chilean forearc, this region cannot serve as the radiogenic source of the dust, since its $^{207}Pb/^{204}Pb$ isotope ratios are too low (Fig. 6b). The $^{208}Pb/^{204}Pb$ isotope ratios are, overall, also too unradiogenic (Fig. 7b). The average $^{206}Pb/^{204}Pb$ isotopic composition of the SVZ, located further to the south, is too low, and the $^{207}Pb/^{204}Pb$ and $^{208}Pb/^{204}Pb$ too high to be the radiogenic end-member (Figs. 6b and 7b).

Although the South CVZ is characterized by suitable radiogenic Pb isotope ratios, its average composition does not exactly match the Site 495 and Site 1256 Pb isotopic arrays. Detritus from the South CVZ reaching the eastern Central Pacific thus may either have a slightly different composition than the average composition of the analyzed South CVZ samples or the average particulate matter

reaching the EEP consists of a mixture of CVZ with NVZ debris, in which the South CVZ material dominates the mixture and plots at the enriched end of the sediment array (Figs. 6b and 7b). Such a mixture in the eastern tropical Pacific waters is very likely based on the prevailing wind and ocean surface current system along western South America (Fig. 1b).

For the studied EEP sediments, we thus conclude that the South CVZ has been the dominant source of radiogenic Pb, complemented by minor admixture of NVZ detritus (Figs. 6b and 7b). Impacts of the Transitional and North CVZ on the radiogenic component, if any, are only subordinate, since potential detrital contributions most likely have been overwhelmed by dust input from the South CVZ (see Section 5.2.2). The exact proportion of NVZ detritus cannot be calculated reliably due to uncertainties in the exact composition of the material transported northward (by ocean currents; see Section 5.2.2) along the western margin of South America to the EEP.

Continuous supply of radiogenic Pb from Southern Hemisphere Andean Arc sources is reasonable for the EEP sediments deposited south of the ITCZ, i.e., prior to 6 Ma. However, given the reversal of the long-term Pb isotopic trend from ~6 to 4 Ma onwards (Fig. 4), it is unlikely that the delivery of Andean Arc Pb maintained its importance during the younger depositional history. Slowly diminishing the supply of sediments from the Andean sources after 6–4 Ma would result in an increase in the relative proportion of hydrothermal detritus from the EPR, which may have caused a reversal in the trend toward the depleted end-member(s). Given the fairly low and overall invariant mass accumulation rate of metalliferous material and the concurrent steady increase of terrigenous matter deposited at Site 1256 during the past 5–6 million years (Wilson et al., 2003), it is unlikely that the proportion of hydrothermal detritus from the EPR MORB source significantly increased in comparison to continental dust sources. Furthermore, the end of superfast EPR spreading at ~11 Ma (Geldmacher et al., 2013) most likely led to decreasing hydrothermal activity in the EEP, as the spreading rate correlates positively with the spatial density of hydrothermal vent sites along a ridge (Baker and German, 2004). This indicates less hydrothermal plumes at the EPR in the aftermath of the superfast spreading period. Therefore, we propose that an additional, less radiogenic source from the Northern Hemisphere has to be taken into account after the sites left the Southern Hemisphere wind and ocean current system. Considering that the sediment samples continue to plot on the pre-6 Ma array after the reversal in the isotopic trend at 6–4 Ma (Figs. 6 and 7), a less radiogenic source with an average Pb isotopic composition on the sediment array needs to be invoked. Sources in south and central Mexico (western Oaxaca and TMVB) have average Pb isotopic compositions falling on (western Oaxaca) or very close (TMVB) to the composition of the youngest sediments at both sites and thus likely served as the dominant Northern Hemisphere sources that caused the reversal in the Pb isotopic trends (Figs. 6a and 7a).

In summary, the sediments deposited on the Cocos Plate seafloor are a mixture between the unradiogenic Pb component of the EPR-related Cocos Plate basement, which has been present throughout the 23 Ma depositional history of our sediments and a radiogenic Pb component originating from the Northern and Central Andes, primarily the South CVZ, until ~6–4 Ma ago. Subsequently, the Andean Arc component in the Sites 495 and 1256 marine sediments was partially replaced by material from southern Mexican igneous complexes, causing the sediments to become overall less radiogenic in their Pb isotopic composition again.

5.2. Transport pathways of Pb to the studied sites of deposition

5.2.1. The submarine advection of hydrothermal Pb

Most metals leached from the oceanic crust are precipitated at high-temperature hydrothermal vents near the spreading centers when the hydrothermal fluids interact with cold seawater (e.g., Hannington, 2013). However, a significant amount of the metalliferous material is entrained in buoyant plumes, which may rise several hundreds of meters above the vent sites (e.g., Lupton and Craig, 1981; Lupton, 1995). During their ascent, the plumes increasingly mix with the surrounding seawater, while being transformed to non-buoyant plumes that may then expand laterally from the ridge crest over distances of up to several thousand kilometers (e.g., Lupton and Craig, 1981; Edmond et al., 1982; Lupton, 1995; Lupton et al., 2004; Fitzsimmons et al., 2014). The material in the hydrothermal plumes largely consists of Fe-oxyhydroxide particles and dissolved metals derived from disaggregation of sulfide minerals (e.g., Hannington, 2013), which is also reflected by the composition of the resulting metalliferous sediments (e.g., Boström and Peterson, 1969; Barrett et al., 1987). The Fe-oxyhydroxides continuously scavenge dissolved metals from the ambient water, while being transported in the non-buoyant plumes (e.g., Gurvich, 2006) leading to dilution of the hydrothermal signal with time and distance from the vent sites.

Based on Pb isotopes, Barrett et al. (1987) demonstrated that mid-ocean ridge (MOR) hydrothermal Pb was present in significant amounts in the metalliferous component of Pacific Basin sediments at a distance of ~1000 km from the EPR at ~20°S. Continuous distal advection of MOR-derived hydrothermal Pb, up to ~1300 km for Site 1256 and ~1500 km for Site 495 (Fig. 1a), is evident from the excellent overall correlations in Pb–Pb isotope space in our data requiring a common unradiogenic component (Figs. 6 and 7). This demonstrates that hydrothermal particulate Pb has been transported from the EPR to the Guatemala Basin by eastward-flowing bottom currents, probably similar to those ones crossing the present-day northern EPR from the west (reviewed by Lonsdale, 1976; Fig. 3b), throughout the recorded sedimentation history. Due to increasing admixture of ambient (detritus-enriched) seawater and the mixing of water masses in general, the Galápagos plume-related differences in Pb isotopic compositions between the distinct EPR sources at each drill site (see Section 5.1.1) vanished at distances exceeding ~900 km (Fig. 5). Our interpretation of eastward advection and deposition of MOR hydrothermal Pb is consistent with

contour maps of metalliferous sediment from Boström and Peterson (1969), which were later confirmed by Lyle (1992), showing northeastward extending sediment lobes in the Guatemala Basin with decreasing proportions of metalliferous matter with increasing distance from the EPR.

In summary, the well-defined linear Pb isotopic correlation strongly suggests that deep currents have continuously transported hydrothermal particulate matter to the east in the EEP since the beginning of marine sedimentation on the Cocos Plate at ~23 Ma. Furthermore, this implies that hydrothermally derived non-buoyant plumes may form an important mechanism for transporting hydrothermal particles with unradiogenic (MORB-type) Pb over millions of years. Therefore, the deep ocean current patterns most likely have not changed considerably in the EEP during this time interval. Moreover, a gradual Late Miocene to Pliocene closing of the Central American Seaway (reviewed by Molnar, 2008) does not appear to have had a major impact on the deep circulation in the central and eastern Pacific. Alternatively, an Early Miocene disappearance of the Pacific–Caribbean deep-water connection may have led to stable deep-water circulation shortly after the onset of the Panama–South America convergence, which has recently been dated at 25−23 Ma (Farris et al., 2011). The latter scenario is in line with cessation of deep-water communication and leaving behind only shallow marine connections by c. 15−13 Ma, as suggested by Montes et al. (2012a, 2012b, 2015).

5.2.2. Airborne and riverine input from the Southern Hemisphere

While the unradiogenic Pb end-member of the sediment arrays originated in the ocean, the radiogenic Pb end-member was most likely introduced into the surface waters by detrital supply from the Andean NVZ and CVZ, primarily the South CVZ, prior to ~6–4 Ma ago and increasing inputs from southern Mexican igneous complexes thereafter. At least for the latest Quaternary, the South CVZ source has also served as the radiogenic end-member at more westerly equatorial ODP Site 849 (Fig. 1a) (Pichat et al., 2014). This site has always been located south of the ITCZ, i.e., within the region governed by the Southeast Trade Winds (Fig. 2a). Today, it is situated at ~110°W and hence at a distance of approximately 2400 km from the closest continent, and it has never been located closer than ~2000 km to any continental landmass, based on its paleotrack (Fig. 1a). Thus, Site 849 has always been remote from any hemipelagic influence, in contrast to sites further east (Rea, 1994, and references therein). Indeed, Hovan (1995) demonstrated that EEP sites drilled along 110°W have been controlled by pelagic sedimentation, i.e., eolian supply has dominated over time. In view of this result, Pichat et al. (2014) invoked the Southeast Trade Winds (STW) as the main input pathway of detrital Pb for Site 849. Since Sites 495 and 1256 indicate a supply from a similar radiogenic end-member over the entire Neogene and Quaternary, the STW are also likely to have transported continental arc-derived Pb from the South CVZ to these sites, at least as long as they were located within the ITCZ or south of it. Input via the STW is reasonable taking into account the distance between the studied sites and the South CVZ source of ~4200–4600 km (Fig. 1b). Consequently, we ascribe only a minor role to the South Equatorial Current (Figs. 1b and 3a) for delivery of detrital Pb from the South CVZ to the EEP drill sites due to the high potential of dust emission in the southern Central Andean source area.

The origin of the dust supplied via the STW is currently located between 20°S and 30°S (Fig. 1b) in the coastal region occupied by the Atacama Desert, presently yielding the highest dust production rates in South America (e.g., Ginoux et al., 2012). Strong aridity in the South CVZ region commenced during the Early to Middle Miocene coinciding with orogenic uplift in this area (e.g., Alpers and Brimhall, 1988; Dunai et al., 2005; Rech et al., 2006). The transition of semiarid to extremely arid conditions in the region of the present-day Atacama Desert took place between 25 and 15 Ma (e.g., Dunai et al., 2005; Rech et al., 2006, 2010; Evenstar et al., 2009). An Early Miocene onset of arid conditions in the southern Central Andes (South CVZ) and important eolian dust contributions from this source area are consistent with our data (see Section 5.5). Long-term aridity in the area of the South CVZ explains why this source has dominated over other possible Andean sources over the last ~23 Ma of sedimentation in the EEP. The results of the present study also suggest that the Neogene-Quaternary sedimentation in the Guatemala Basin lacks any significant contribution of detrital Pb from the Southern Volcanic Zone (SVZ; see Section 5.1). This is in contrast to the results of Pichat et al. (2014), who suggested that the SVZ serves as the unradiogenic end-member for Site 849 bulk sediments, resulting from shifting wind patterns between glacial and interglacial cycles in the Late Pleistocene southern South America. We assume that such a fluctuation did not have an impact on the pre-Quaternary eastern equatorial Pacific or the lower temporal resolution of our study does not allow detection of provenance changes on time scales of tens of thousands of years, in particular during the Quaternary. Alternatively, the lack of SVZ contribution at Sites 495 and 1256 could also reflect the far more easterly locations compared to Site 849, leading to present-day distance of ~2300 km (Fig. 1). Backtracking the Southeast Trade Winds at more easterly Sites 495/1256 points to a source further north in South America, which is not consistent with the SVZ.

In contrast to the Atacama area, northwestern South America, i.e., the region occupied by the Northern Volcanic Zone (NVZ), is presently characterized by high annual precipitation rates, leading to tropical climate at higher altitudes with rainforests and subordinate savanna habitats under temperate conditions (e.g., Andriessen et al., 1993; García, 1994). This has caused intense mass wasting to the trench of the Andean subduction zone in this area (reviewed by Stern, 2004). Both faunal and vegetational reconstructions have yielded similar climatic conditions throughout the Neogene and the Pliocene with mainly tropical forests and minor woodland savannas (reviewed and/or reconstructed by Webb, 1978; Janis, 1993; Pound et al., 2011, 2012). Significant eolian Pb input from the Northern Andes is thus unlikely, since there is a strong negative correlation of the humidity of an area and its potential to emit

dust to the atmosphere (Rea, 1994, and references therein). We therefore suggest that continental runoff coupled with subsequent advection in the South Equatorial Current system is the principal mechanism for transporting a Northern Andean Pb component to the eastern equatorial Pacific. The main uplift phase of the Northern Andes, which corresponds to the NVZ, began after ~12 Ma (e.g., Gregory-Wodzicki, 2000; Hoorn et al., 2010). Milliman and Syvitski (1992) stressed that, compared to large streams, smaller mountainous rivers of active plate margins may supply greater proportions of their sediment loads straight to the ocean. A major riverine pathway may have also existed through the possible connection of the widespread proto-Amazon river and wetland system to the Pacific along the southern part of the Northern Andes (reviewed by Hovikoski et al., 2010), prior to establishment of the Amazon drainage toward the Atlantic between 12 and 10 Ma (Dobson et al., 2001; Figueiredo et al., 2009). Nevertheless, based on our Pb isotope data correlation (Figs. 6 and 7), the ocean surface stream pathway is less efficient compared to the eolian supply to the EEP, since the overall contribution of the NVZ source is of minor significance.

The high potential of the Atacama Desert to emit dust to the atmosphere within the Southeast Trade Wind zone turns the South CVZ into the predominant detrital source in the Central Andes. It seems to overwhelm both the Transitional and North CVZ in terms of detrital input into the eastern Central Pacific, as reflected by the Pb isotopic compositions (Figs. 6b and 7b). Furthermore, the present-day region of the North CVZ is characterized by lesser aridity than the southern Central Andes (Montgomery et al., 2001; Garreaud et al., 2003; Hartley, 2003). The modern climatic pattern of the Central Andes has been existent since the beginning of the Neogene (Hartley, 2003). Thus, the amount of continental detritus provided from the northern Central Andes to Sites 495 and 1256 is assumed to have been generally low over the studied period of time.

5.2.3. Subaerial and submarine delivery of detritus from southern Mexico

The Paleogene igneous complexes of southern Mexico (e.g., Oaxaca) widely crop out in an area extending along the Pacific coast from ~95 to 103°W and far north to the Trans-Mexican Volcanic Belt (TMVB) at c. 18°N (Martiny et al., 2000). Continental runoff and subsequent mass wasting at the margin as well as dust transport via the Northeast Trade Winds are regarded as the major mechanisms bringing terrigenous matter to the ocean in this area. The relative roles of the two transport mechanisms most likely changed, since Mexico has been subject to different climates during the Neogene to Quaternary. As shown by paleoecological studies, a humid climate in the Early to Middle Miocene, promoting tropical woodlands and forests, gradually transformed into a semiarid setting with rainy seasons hosting subtropical savannas during the Latest Miocene and Pliocene (e.g., Webb, 1977; Janis, 1993; Pound et al., 2011, 2012; Eronen et al., 2012). Therefore, a combination of riverine and eolian Pb supply to the eastern equatorial Pacific was likely, favoring an increasing contribution of eolian dust over time in view of the declining average humidity in the area. Once the sampling sites reached the paleo-ITCZ in the Late Miocene to Pliocene (Fig. 2), zonal and meridional winds within the Northeast Trade Wind belt started to have an impact on the study area. However, while possible supply of far-traveled TMVB detritus may strongly depend on the strength of eolian transport, the southern Mexican geological units are additionally subject to a runoff and mass wasting component, facilitating input of detrital material from that near coastal area. Thus, in comparison with the ~500 km distant central Mexican arc, it is generally more likely that significant amounts of detritus were delivered to the EEP from the coastal igneous units, possibly reflecting enhanced riverine input after major uplift in that area, which lasted from the Late Oligocene to Middle Miocene (Morán-Zenteno et al., 1996).

The modern oceanic surface circulation of the easternmost tropical Pacific could also have contributed to ubiquitous distribution of southern Mexican detritus within the Guatemala Basin (Fig. 3a). At near-surface to intermediate water depths, nepheloid layers of detrital suspension load may have propagated as suspension currents, which have been interpreted to represent terrigenous matter detached from continental slope turbidite currents transporting continental particles across deep-sea trenches into the open ocean (Heinemann and Füchtbauer, 1982; Shiki et al., 1982). In addition, mixing of different water masses may dominate the present deep-water circulation (Fig. 3b), given the southward lobe of terrigenous material obviously entraining detritus from the Mexican continental slope along the eastern flank of the EPR (Lyle, 1992). This detritus may subsequently be transported to the studied sites of sedimentation by eastward bottom currents (Fig. 3b). The present study now geochemically corroborates the existence of such a counter-clockwise deep-water flow during at least the past ~7–6 million years, which has been proposed by Lyle (1992) for the present-day EEP, since the proximal southern Mexican igneous belts have obviously also played a role as a radiogenic source end-member for the dissolved seawater Pb as recorded by northern EEP Fe–Mn crust GMAT 14D throughout its growth history (Figs. 6a and 7a).

5.3. Why has the Central Andean Arc remained a significant source of radiogenic Pb north of the ITCZ?

Although the most recent sediments at both Site 495 and Site 1256 have a composition almost identical to the average western Oaxaca (±TMVB) igneous complexes, the decreasing Pb isotope ratios after ~6–4 Ma ago clearly indicate a decreasing input from the South CVZ after both studied sites left the Southern Hemisphere circulation. Two different mechanisms could be invoked to explain how significant amounts of sediments from the southern Hemisphere continued to reach the drill sites after they crossed the ITCZ (Figs. 6 and 7). First, Site 1256 is presently still located within the northernmost part of the latitudinal zone of annual ITCZ shifts (Fig. 2a) suggesting that eolian contributions from the Southern Hemisphere have always been possible. Second, Lyle (1992) revealed a sediment lobe of considerable terrigenous deposition

extending from ~12°S to an area north of the Galápagos triple junction at ~5°N in a SE–NW direction (Fig. 3b), which he proposed to indicate detritus transported and accumulated by the Southeast Trade Winds. Thus, eastward surface and northeastward bottom currents could have carried wind-blown particles from South America to the studied sites of deposition. It has additionally been demonstrated that the seawater record of Fe–Mn crust GMAT 14D continuously shared the same Pb isotopic end-members as the bulk sediments over the past 7–6 million years (Figs. 6 and 7), although it has always been located north of the ITCZ (Fig. 2b). The relatively constant Pb isotopic composition of Fe–Mn crust GMAT 14D (Fig. 4) contrasts with the trend to less radiogenic Pb isotopic compositions of Sites 495 and 1256, approaching the composition of GMAT 14D over the last ~6–4 Ma. This shows that the studied drill sites and the location of GMAT 14D finally shared the same atmospheric and ocean surface circulation system, i.e., the Northern Hemisphere domain. In turn, this demonstrates that GMAT 14D was not exposed to the same atmospheric and ocean surface system as the two drill sites prior to ~4 Ma (Figs. 2 and 3a). Nonetheless, the small temporal variability of the Pb isotopic evolution of the GMAT 14D record, which is identical to that of the leachate data obtained at Site 1256 over the past 7–6 Myr, indicates well-mixed deep waters supplied by Pb from all sources relevant to the study area (Figs. 4, 6 and 7). This points to a persistent and efficient deep-water connection between Site 1256, Site 495, and Fe–Mn crust GMAT 14D, at least since ~6 Ma (see Section 5.2). The existence of such a suggested gyre-like circulation (Fig. 3b) also implies that any detrital Pb isotopic variability in the study area results from changes in the supply of lithogenic matter within the eastern Central Pacific independently of any potential changes in oceanic circulation related to the closing Panama gateway, supporting the results of Frank et al. (1999).

5.4. Why have Central America and the Galápagos Archipelago been insignificant sediment input sources to the Guatemala Basin?

It is a somewhat surprising result that sediment input from Central America and the Galápagos Archipelago to the eastern equatorial Pacific near our study sites was insignificant during the Neogene and Quaternary. Prior to ~7–6 Ma, both sites were located south of the ITCZ and thus eolian input from Central America was unlikely at that time. However, since Central America has obviously not been a major source of sediments at Sites 495 and 1256 after the sites crossed the ITCZ either, reasons other than tectonic migration must also have been involved. Central America was subject to a tropical climate during the Miocene and Early Pliocene, in which humid conditions prevailed and rainforests and subtropical vegetation covered much of the land surface (reviewed by Webb, 1978; Janis, 1993; Woodburne, 2010; Pound et al., 2012). Drier savanna-like habitats have been suggested for the Early Pliocene and the Pleistocene prior to the onset of the mainly tropical Holocene environment (Woodburne, 2010, and references therein). Given this climatic evolution, an eolian contribution of Pb from Central America was unlikely during the Neogene, when Central America generally had a lowland character or was not exposed except for the Central American Arc volcanoes (Whitmore and Stewart, 1965; Webb, 1978, and references therein; Kirby and MacFadden, 2005; Farris et al., 2011; Coates and Stallard, 2013, and references therein). In the Late Miocene, uplift created highlands, such as in northwestern Central America, which possibly resulted from slab detachment (Rogers et al., 2002). Similarly, Pleistocene tectonic uplift of the Isthmus of Panama (O'Dea et al., 2012) due to collision of the Cocos Ridge with southern Central America also caused uplift and closing of the seaway to the Caribbean (Hoernle et al., 2002). Although significant relief is likely to have formed by the Latest Miocene in the highland area of present-day Honduras (Rogers et al., 2002), it was obviously not sufficient to establish considerable runoff toward the study area and thus the hemipelagic input from the northwestern Central American Volcanic Arc region during most of the studied period of time was limited. In addition, regionally exposed continental basement areas of the Chortís Block, which may have provided detrital particles with high Pb concentrations of up to ~22 ppm to the marine sediments (Guatemala metamorphic basement; Heydolph et al., 2012), likely have not contributed a significant proportion of the river load drained into the EEP. Potential runoff from Central America has preferentially drained mafic ophiolitic terranes being accreted along the Pacific seaward side of the Chortís Block that are characterized by low Pb concentrations (e.g., Hauff et al., 2000; Geldmacher et al., 2008) and relatively unradiogenic Pb isotopic compositions (see Section 5.1.1).

Volcanic debris from the nearby Galápagos Islands has probably been supplied by the same atmospheric (Southeast Trade Winds) and oceanic (South Equatorial Current system) pathways as those providing detrital material from the continental margin of western South America (Figs. 2 and 3). However, an impact of material supply by the Galápagos Archipelago on the Pb isotope record of studied drilling sites has been insignificant, since local detrital input from this area appears to have been overwhelmed by that of the geographically and volumetrically much larger Andean Arc sources to the east and southeast.

5.5. Paleoclimatic implications of the eastern Central Pacific Pb isotopic evolution

Three main factors have controlled the temporal variability in the Pb isotope data from Sites 495 and 1265: plate tectonics, oceanography, and climate. The tectonic motion of the Cocos Plate has carried the drill sites away from their respective formation areas at the EPR since ~23–22.5 (Site 495) and ~15.2 Ma (Site 1256). As the hydrothermal systems providing the MORB-like Pb isotopic material to the sediments are associated with the EPR, transport away from the EPR resulted in a reduction of MORB-type Pb being contributed to the sediments with decreasing age of the sediments (Figs. 4, 6 and 7). The present study, however, also shows that

this MORB signal is still detectable after the sites have been carried >1000 km from the ridge axis, reflecting steady-state oceanographic conditions in the eastern Central Pacific with persistent eastward deep-water circulation over millions of years. The contribution of a second, radiogenic Pb isotope source from the Central Andes (South CVZ) resulted from arid climatic conditions creating the Atacama Desert in the Early Miocene (Rech et al., 2006) combined with the prevailing south trade wind patterns (see Section 5.2.2). Ocean currents also appear to have transported material form the northern Andes (NVZ) to the study sites. The airborne and riverine sediment sources in the Southern Hemisphere have provided a continuous supply of particles with radiogenic Pb that systematically replaced the unradiogenic MORB Pb component as the sites moved progressively away from the EPR. The decrease in contributions from the hydrothermal source can explain both the systematic increase in radiogenic Pb isotopic composition through time until ~6–4 Ma ago (Fig. 4) and the largely two-component linear mixing arrays on Pb–Pb isotope diagrams (Figs. 6 and 7). Therefore, the Pb isotopic evolution to more radiogenic compositions between 23 and 6–4 Ma ago was largely controlled by the interplay of unradiogenic mantle-derived Pb with radiogenic continent-derived Pb. The <6 Ma part of the Pb isotopic evolution ultimately resulted from crossing the ITCZ and thus a decrease in the input of Andean Pb and an increase in the contribution from Mexican sources over time. Southern Mexico underwent significant aridification during the Neogene (Eronen et al., 2012) making eolian transport of sediments more likely in the Pliocene and Quaternary. Taking into account the increasing Late Neogene supply of terrigenous material to the EEP (Wilson et al., 2003), the stagnant or decreasing Pb isotope ratios of the post-6 Ma period (Fig. 4) require admixture of material from a less radiogenic Northern Hemisphere dust source that is suggested to be represented by igneous complexes of semiarid southern Mexico coastal areas (e.g., Oaxaca; Figs. 6a and 7a). Crossing of the ITCZ gave rise to the final decrease of Pb isotope ratios toward the composition of the northerly Fe–Mn crust GMAT 14D (Fig. 4), which is located in the northernmost part of the study area, closest to the southern Mexican source (Fig. 1a). Hence, the post-6 Ma isotope record reflects the southward shift of the ITCZ as a consequence of Neogene cooling, inferring (1) an ITCZ paleolatitude around 9°N at 6 Ma marked by the transition in the Pb isotopic trend of the studied sediments and (2) reunification of both studied sites under a common atmospheric domain after ~3 Ma (Fig. 2b).

6. CONCLUSIONS

We have reconstructed the Pb isotopic evolution of sediment supply for DSDP Site 495 and ODP/IODP Site 1256 in the eastern equatorial Pacific (EEP) over the past 23 million years covering the entire Neogene-Quaternary tectonic movement of the Cocos Plate MORB basement from its formation at the East Pacific Rise (EPR) spreading center to its arrival at the Central American subduction zone. The data form well constrained mixing arrays reflecting particulate inputs from three major sources: depleted mantle-derived Pb from the EPR hydrothermal systems, enriched continental arc Pb originating from a mixture of terrigenous material from the Andean Arc (the Northern and south Central Volcanic Zones) and the southern Mexican igneous belts (e.g., coastal area of Oaxaca). The major carrier of the hydrothermal Pb has been plumes originating from EPR hydrothermal systems distributed by deep-water currents. Transport by winds has been the major pathway of detrital sediment supply to the EEP, particularly from the Central Andes and southern Mexico, whereas direct continental runoff and ocean surface currents have only played a subordinate role. Inputs of sediments from the most proximal potential sources in northwestern Central America and the Galápagos Archipelago were relatively insignificant due to a combination of factors including lack of subaerially exposed surface area (Galápagos Archipelago) and limited topography as well as absence of sandy deserts from which wind-blown sediments could be derived (Central America), compared to extensive arid areas largely free of vegetation (Central Andean and Mexican sources).

The temporal evolution of the EEP Pb isotope record has primarily been driven by the northward tectonic migration of the studied drill sites on the Cocos Plate (1) away from the East Pacific Rise over the past 23 Ma and (2) northward crossing of the southward shifting Intertropical Convergence Zone (ITCZ) between ~6 and ~3 Ma ago. As the sites moved away from the EPR, the amount of hydrothermal Pb supplied to the sediments decreased continuously over time. In contrast, the relative proportion of continental material from the Southern Hemisphere (Northern and Central Andes) increased as reflected by a systematic change in the Pb isotopic composition to more radiogenic compositions until ~6 Ma. After the sites crossed the ITCZ between ~6 and ~3 Ma ago, the Pb isotope data indicate that the supply of Southern Hemisphere material declined in favor of Northern Hemisphere sources (primarily the igneous complexes of southern Mexico).

The constant delivery of EPR-derived hydrothermal Pb to the drill sites strongly implies far-reaching and continuous lateral advection of hydrothermal plume matter by deep-water currents over distances of more than 1000 km toward the east. In addition, we suggest that winds have transported dust from the Southern Hemisphere to the Galápagos triple junction region and then the detritus has been carried by deep-water currents to the sites of sedimentation. The data indicate that the general deep-water circulation system in the central and eastern equatorial Pacific has been reasonably stable over the last ~23 million years despite large paleoceanographic changes linked to Central American Seaway closure. The bottom water Pb isotopic compositions extracted in addition to the detrital data support the existence of an abyssal gyre circulation in the Guatemala Basin, efficiently connecting the locations of Sites 1256 and 495 and of Fe–Mn crust GMAT 14D, leading to a pronounced similarity of each Pb isotope record since at least ~6 Ma.

ACKNOWLEDGMENTS

We are grateful to S. Hauff, J. Heinze, and A. Klügel for valuable analytical support, as well as to S. Duggen for fruitful discussions. Constructive reviews by D. Wilson and three anonymous reviewers are gratefully acknowledged. Furthermore, we sincerely thank J. Blichert-Toft for considerate editorial handling. M. Norman is acknowledged for editorial support. This research used samples provided by Integrated Ocean Drilling Program (IODP). The present study and T.W.H. were funded by the Deutsche Forschungsgemeinschaft (DFG) IODP/ODP priority program (SPP 527) grants HO1833/16-1 and HO1833/18-1.

APPENDIX A. SUPPLEMENTARY DATA

Supplementary data associated with this article can be found, in the online version, at http://dx.doi.org/10.1016/j.gca.2016.05.003.

REFERENCES

Abouchami W., Goldstein S. L., Gazer S., Eisenhauer A. and Mangini A. (1997) Secular changes of lead and neodymium in central Pacific seawater recorded by a Fe–Mn crust. *Geochim. Cosmochim. Acta* **61**(18), 3957–3974. http://dx.doi.org/10.1016/S0016-7037(97)00218-4.

Alpers C. N. and Brimhall G. H. (1988) Middle Miocene climatic change in the Atacama Desert, northern Chile: evidence from supergene mineralization at La Escondida. *Geol. Soc. Am. Bull.* **100**(10), 1640–1656, 10.1130/0016-7606(1988)100<1640:MMCCIT>2.3.CO;2.

Alvarado G. E., Dengo C., Matens U., Bundschuh J., Aguilar T. and Bonis S. B. (2007) Stratigraphy and geologic history. In *Central America: Geology, Resources and Hazards* (eds. J. Bundschuh and G. E. Alvarado). Taylor and Francis, London, pp. 345–394.

Andriessen P., Helmens K. F., Hooghiemstra H., Riezebos P. A. and Van der Hammen T. (1993) Absolute chronology of the Pliocene-Quaternary sediment sequence of the Bogota area, Colombia. *Quaternary Science Reviews* **12**(7), 483–501. http://dx.doi.org/10.1016/0277-3791(93)90066-U.

Baker E. T. and German C. R. (2004) On the global distribution of hydrothermal vent fields. In *Mid-Ocean Ridges, Geophysical Monograph (148)* (eds. C. R. German, J. Lin and L. M. Parson). American Geophysical Union, Washington, pp. 245–266. http://dx.doi.org/10.1029/148GM10.

Baker J. A., Peate D. W., Waight T. E. and Meyzen C. (2004) Pb isotopic analysis of standards and samples using a 207Pb–204Pb double spike and thallium to correct for mass bias with a double-focusing MC-ICP-MS. *Chem. Geol.* **211**, 275–303.

Baker J. A., Peate D. W., Waight T. E. and Thirlwall M. F., et al. (2005) Reply to the: Comment on "Pb isotopic analysis of standards and samples using a 207Pb–204Pb double spike and thallium to correct for mass bias with a double focusing MC-ICP-MS" by Baker. *Chem. Geol.* **217**, 175–179.

Barrett T. J., Taylor P. N. and Lugoqski J. (1987) Metalliferous sediments from DSDP Leg 92: The East Pacific Rise transect. *Geochim. Cosmochim. Acta* **51**(9), 2241–2253. http://dx.doi.org/10.1016/0016-7037(87)90278-X.

Basak C. and Martin E. E. (2013) Antarctic weathering and carbonate compensation at the Eocene–Oligocene transition. *Nat. Geosci.* **6**(2), 121–124. http://dx.doi.org/10.1038/ngeo1707.

Berggren W. A., Hilgen F. J., Langereis C. G., Kent D. V., Obradovich J. D., Raffi I., Raymo M. E. and Shackleton N. J. (1995a) Late Neogene chronology: new perspectives in high-resolution stratigraphy. *Geol. Soc. Am. Bull.* **107**(11), 1272–1287. http://dx.doi.org/10.1130/0016-7606(1995)107<1272:LNCNPI>2.3.CO;2.

Berggren W. A., Kent D. V., Swisher C. C. and Aubry M.-P. (1995b) A revised Cenozoic geochronology and chronostratigraphy: geochronology, time scales, and global stratigraphic correlation. In *Geochronology*, vol. 54 (ed. Berggren), pp. 129–212.

Boström K. and Peterson M. N. A. (1969) The origin of aluminum-poor ferromanganoan sediments in areas of high heat flow on the East Pacific Rise. *Mar. Geol.* **7**(5), 427–447. http://dx.doi.org/10.1016/0025-3227(69)90016-4.

Broecker W., Peng T. H. and Beng Z. (1982) *Tracers in the Sea*. Lamont-Doherty Geological Observatory, Columbia University, Palisades, NY.

Cande S. C. and Kent D. V. (1995) Revised calibration of the geomagnetic polarity timescale for the Late Cretaceous and Cenozoic. *J. Geophys. Res. Solid Earth* **100**(B4), 6093–6095. http://dx.doi.org/10.1029/94JB03098.

Castillo P. R., Klein E., Bender J., Langmuir C., Shirey S., Batiza R. and White W. (2000) Petrology and Sr, Nd, and Pb isotope geochemistry of mid-ocean ridge basalt glasses from the 11 45′N to 15 00′N segment of the East Pacific Rise. *Geochem. Geophys. Geosyst.* **1**(11), 1–40. http://dx.doi.org/10.1029/1999GC000024.

Chen J. H., Wasserburg G. J., von Damm K. L. and Edmond J. M. (1986) The U–Th–Pb systematics in hot springs on the East Pacific Rise at 21 N and Guaymas Basin. *Geochim. Cosmochim. Acta* **50**(11), 2467–2479. http://dx.doi.org/10.1016/0016-7037(86)90030-X.

Chow T. J. and Patterson C. C. (1962) The occurrence and significance of lead isotopes in pelagic sediments. *Geochim. Cosmochim. Acta* **26**(2), 263–308. http://dx.doi.org/10.1016/0016-7037(62)90016-9.

Coates A. G. and Stallard R. F. (2013) How old is the Isthmus of Panama?. *Bull. Mar. Sci.* **89**(4) 801–813. http://dx.doi.org/10.5343/bms.2012.1076.

Coulbourn W. T., Hesse R., Azema J. and Shiki T. (1982) A summary of the sedimentology of DSDP Leg 67 sites: the Middle America trench and slope off Guatemala – an active margin transect. In *Initial Reports of the Deep Sea Drilling Project covering Leg 67 of the cruises of the drilling vessel Glomar Challenger, Initial Reports of the Deep Sea Drilling Project, Manzanillo, Mexico to Puntarenas, Costa Rica* (ed. S. Orlofsky), pp. 759–774.

DeMets C., Gordon R. G., Argus D. F. and Stein S. (1990) Current plate motions. *Geophys. J. Int.* **101**(2), 425–478. http://dx.doi.org/10.1111/j.1365-246X.1990.tb06579.x.

Dobson D. M., Dickens G. R. and Rea D. K. (2001) Terrigenous sediment on Ceara Rise: a Cenozoic record of South American orogeny and erosion. *Palaeogeogr. Palaeoclimatol. Palaeoecol.* **165**(3–4), 215–229. http://dx.doi.org/10.1016/S0031-0182(00)00161-9.

Dunai T. J., González López Gabriel. A. and Juez-Larré J. (2005) Oligocene–Miocene age of aridity in the Atacama Desert revealed by exposure dating of erosion-sensitive landforms. *Geology* **33**(4), 321. http://dx.doi.org/10.1130/G21184.1.

Edmond J. M., Von Damm K. L., McDuff R. E. and Measures C. I. (1982) Chemistry of hot springs on the East Pacific Rise and their effluent dispersal. *Nature* **297**(5863), 187–191. http://dx.doi.org/10.1038/297187a0.

Eronen J. T., Fortelius M., Micheels A., Portmann F. T., Puolamaki K. and Janis C. M. (2012) Neogene aridification of the Northern Hemisphere. *Geology* **40**(9), 823–826. http://dx.doi.org/10.1130/G33147.1.

Evenstar L. A., Hartley A. J., Stuart F. M., Mather A. E., Rice C. M. and Chong G. (2009) Multiphase development of the Atacama Planation Surface recorded by cosmogenic 3He exposure ages: implications for uplift and Cenozoic climate change in western South America. *Geology* **37**(1), 27–30. http://dx.doi.org/10.1130/G25437A.1.

Farris D. W., Jaramillo C., Bayona G., Restrepo-Moreno S. A., Montes C., Cardona A., Mora A., Speakman R. J., Glascock M. D. and Valencia V. (2011) Fracturing of the Panamanian Isthmus during initial collision with South America. *Geology* **39** (11), 1007–1010. http://dx.doi.org/10.1130/G32237.1.

Faure G. (2001) *Origin of Igneous Rocks: The Isotopic Evidence*. Springer, Berlin.

Faure G. and Mensing T. M. (2005) *Isotopes: Principles and Applications*, 3rd ed. Wiley, Hoboken, NJ.

Feigenson M. D., Carr M. J., Maharaj S. V., Juliano S. and Bolge L. L. (2004) Lead isotope composition of Central American volcanoes: influence of the Galapagos plume. *Geochem. Geophys. Geosyst.* **5**(6), 1–14. http://dx.doi.org/10.1029/2003GC000621.

Ferrari L., Orozco-Esquivel T., Manea V. and Manea M. (2012) The dynamic history of the Trans-Mexican Volcanic Belt and the Mexico subduction zone. *Tectonophysics* **522–523**, 122–149. http://dx.doi.org/10.1016/j.tecto.2011.09.018.

Figueiredo J., Hoorn C., van der Ven P. and Soares E. (2009) Late Miocene onset of the Amazon River and the Amazon deep-sea fan: evidence from the Foz do Amazonas Basin. *Geology* **37**(7), 619–622. http://dx.doi.org/10.1130/G25567A.1.

Fitzsimmons J. N., Boyle E. A. and Jenkins W. J. (2014) Distal transport of dissolved hydrothermal iron in the deep South Pacific Ocean. *Proc. Natl. Acad. Sci. U.S.A.* **111**(47), 16654–16661. http://dx.doi.org/10.1073/pnas.1418778111.

Flohn H. (1981) A hemispheric circulation asymmetry during Late Tertiar. *Int. J. Earth Sci.* **70**(2), 725–736. http://dx.doi.org/10.1007/BF01822146.

Frank M., Reynolds B. C. and Keith O'Nions R. (1999) Nd and Pb isotopes in Atlantic and Pacific water masses before and after closure of the Panama gateway. *Geology* **27**(12), 1147–1150. http://dx.doi.org/10.1130/0091-7613(1999)027<1147:NAPIIA>2.3.CO;2.

Frank M. (2002) Radiogenic isotopes: tracers of past ocean circulation and erosional input. *Rev. Geophys.* **40**(1). http://dx.doi.org/10.1029/2000RG000094.

Galer S. J. G. (1999) Optimal double and triple spiking for high precision lead isotopic measurement. *Chem. Geol.* **157**, 255–274.

García N. O. (1994) South American climatology. *Quatern. Int.* **21**, 7–27. http://dx.doi.org/10.1016/1040-6182(94)90018-3.

Garreaud R., Vuille M. and Clement A. (2003) The climate of the Altiplano: observed current conditions and mechanism of past changes. *Paleogeogr. Palaeoclimatol. Palaeoecol.* **194**(3054), 1–18. http://dx.doi.org/10.1016/S0031-0182(03)00269-4.

Gazel E., Carr M. J., Hoernle K., Feigenson M. D., Szymanski D., Hauff F. and van den Bogaard P. (2009) Galápagos-OIB signature in southern Central America: mantle refertilization by arc-hot spot interaction. *Geochem. Geophys. Geosyst.* **10**(2), Q02S11. http://dx.doi.org/10.1029/2008GC002246.

Gazel E., Hoernle K., Carr M. J., Herzberg C., Saginor I., van den Bogaard P., Hauff F., Feigenson M. and Swisher C. (2011) Plume-subduction interaction in southern Central America: Mantle upwelling and slab melting. *Lithos* **121**, 117–134.

Geldmacher J., Hoernle K., van den Bogaard Paul., Hauff F. and Klugel A. (2008) Age and geochemistry of the Central American Forearc basement (DSDP Leg 67 and 84): insights into Mesozoic Arc Volcanism and Seamount Accretion on the Fringe of the Caribbean LIP. *J. Petrol.* **49**(10), 1781–1815. http://dx.doi.org/10.1093/petrology/egn046.

Geldmacher J., Höfig T. W., Hauff F., Hoernle K., Garbe-Schönberg D. and Wilson D. S. (2013) Influence of the Galápagos hotspot on the East Pacific Rise during Miocene superfast spreading. *Geology* **41**(2), 183–186. http://dx.doi.org/10.1130/G33533.1.

Ginoux P., Prospero J. M., Gill T. E., Christina Hsu N. and Zhao M. (2012) Global-scale attribution of anthropogenic and natural dust sources and their emission rates based on MODIS Deep Blue aerosol products. *Rev. Geophys.* **50**(3), RG3005. http://dx.doi.org/10.1029/2012RG000388.

Godfrey L. V. (2002) Temporal changes in the lead isotopic composition of red clays: comparison with ferromanganese crust records. *Chem. Geol.* **185**(3–4), 241–254. http://dx.doi.org/10.1016/S0009-2541(01)00406-5.

Goldstein S. L. and Hemming S. R. (2003) Long-lived isotopic tracers in oceanography, paleoceanography, and ice-sheet dynamics. In *Treatise on Geochemistry* (eds. H. D. Holland and K. K. Turekian). Pergamon [Imprint]; Elsevier Science & Technology Books, San Diego, pp. 453–489.

Goss A. R., Perfit M. R., Ridley W. I., Rubin K. H., Kamenov G. D., Soule S. A., Fundis A. and Fornari D. J. (2010) Geochemistry of lavas from the 2005–2006 eruption at the East Pacific Rise, 9 46′N–9 56′N: implications for ridge crest plumbing and decadal changes in magma chamber compositions. *Geochem. Geophys. Geosyst.* **11**(5), Q05T09. http://dx.doi.org/10.1029/2009GC002977.

Gregory-Wodzicki K. M. (2000) Uplift history of the Central and Northern Andes: a review. *Geol. Soc. Am. Bull.* **112**(7), 1091–1105. http://dx.doi.org/10.1130/0016-7606(2000)112<1091:UHOTCA>2.0.CO;2.

Guo Z. T., Ruddiman W. F., Hao Q. Z., Wu H. B., Qiao Y. S., Zhu R. X., Peng S. Z., Wei J. J., Yuan B. Y. and Liu T. S. (2002) Onset of Asian desertification by 22 Myr ago inferred from loess deposits in China. *Nature* **416**, 159–163. http://dx.doi.org/10.1038/416159a.

Gurvich E. G. (2006) *Metalliferous Sediments of the World Ocean: Fundamental Theory of Deep-Sea Hydrothermal Sedimentation*. Springer, Berlin, Heidelberg.

Gutjahr M., Frank M., Stirling C. H., Klemm V., van de Flierdt T. and Halliday A. N. (2007) Reliable extraction of a deepwater trace metal isotope signal from Fe–Mn oxyhydroxide coatings of marine sediments. *Chem. Geol.* **242**(3–4), 351–370. http://dx.doi.org/10.1016/j.chemgeo.2007.03.021.

Gutjahr M., Frank M., Halliday A. N. and Keigwin L. D. (2009) Retreat of the Laurentide ice sheet tracked by the isotopic composition of Pb in western North Atlantic seawater during termination 1. *Earth Planet. Sci. Lett.* **286**, 546–555.

Haley B. A., Frank M., Spielhagen R. F. and Fietzke J. (2008) Radiogenic isotope record of Arctic Ocean circulation and weathering inputs of the past 15 million years. *Paleoceanography* **23**(1), PA1S13. http://dx.doi.org/10.1029/2007PA001486.

Handschumacher D. W. (1976) Post-Eocene plate tectonics of the Eastern Pacific. In *The Geophysics of the Pacific Ocean Basin and Its Margin*, vol. 19 (eds. G. H. Sutton, M. H. Manghnani, R. Moberly and E. U. McAfee). AGU, Washington, DC, pp. 177–202.

Hannington M. D. (2013) The role of black smokers in the Cu mass balance of the oceanic crust. *Earth Planet. Sci. Lett.* **374**, 215–226. http://dx.doi.org/10.1016/j.epsl.2013.06.004.

Hart D. and Miller D. J. (2006) Analysis and correlation of volcanic ash in marine sediments from the Peru margin, ocean drilling program leg 201: explosive volcanic cycles of the North-Central Andes. In *Proceedings of the Ocean Drilling Program, 201 Scientific Results*, vol. 201 (eds. B. B. Jørgensen, S. L. D'Hondt and D. J. Miller).

Hartley A. J. (2003) Andean uplift and climate change. *Geol. Soc. Lond. J.* **160**, 7–10. http://dx.doi.org/10.1144/0016-764902-083.

Hauff F., Hoernle K., Schmincke H. U. and Werner R. (1997) A mid Cretaceous origin for the Galápagos hotspot: Volcanological, petrological and geochemical evidence from Costa Rican oceanic crustal segments. *Geol. Rundsch.* **86**(1), 141–155. http://dx.doi.org/10.1007/PL00009938.

Hauff F., Hoernle K., van den Bogaard P., Alvarado G. and Garbe-Schönberg D. (2000) Age and geochemistry of basaltic complexes in western Costa Rica: contributions to the geotectonic evolution of Central America. *Geochem. Geophys. Geosyst.* **1**(5). http://dx.doi.org/10.1029/1999GC000020.

Heinemann C. and Füchtbauer H. (1982) Insoluble residues of the fine-grained sediments from the Trench transect south of Guatemala, DSDP Leg 67. In *Init. Repts. DSDP, 67* (eds. J. Aubouin and R. von Huene, et al.). U.S. Govt. Printing Office, Washington, pp. 497–506. http://dx.doi.org/10.2973/dsdp.proc.67.117.1982.

Henderson G. M. and Maier-Reimer E. (2002) Advection and removal of ^{210}Pb and stable Pb isotopes in the oceans: a general circulation model study. *Geochim. Cosmochim. Acta* **66**(2), 257–272. http://dx.doi.org/10.1016/S0016-7037(01)00779-7.

Heydolph K., Hoernle K., Hauff F., van den Bogaard Paul., Portnyagin M., Bindeman I. and Garbe-Schönberg D. (2012) Along and across arc geochemical variations in NW Central America: Evidence for involvement of lithospheric pyroxenite. *Geochim. Cosmochim. Acta* **84**, 459–491. http://dx.doi.org/10.1016/j.gca.2012.01.035.

Hoernle K. and Tilton G. (1991) Sr-Nd-Pb isotope data for Fuerteventura (Canary Islands) basal complex and subaerial volcanics: applications to magma genesis and evolution. *Schweiz. Mineral. Petrogr. Mitt.* **71**, 5–21.

Hoernle K., Abt D. L., Fischer K. M., Nichols H., Hauff F., Abers G. A., van den Bogaard Paul., Heydolph K., Alvarado G., Protti M. and Strauch W. (2008) Arc-parallel flow in the mantle wedge beneath Costa Rica and Nicaragua. *Nature* **451**(7182), 1094–1097. http://dx.doi.org/10.1038/nature06550.

Hoernle K., Hauff F., Kokfelt T. F., Haase K., Garbe-Schönberg D. and Werner R. (2011) On- and off-axis chemical heterogeneities along the South Atlantic Mid-Ocean-Ridge (5–11 S): shallow or deep recycling of ocean crust and/or intraplate volcanism? *Earth Planet. Sci. Lett.* **306**(1–2), 86–97. http://dx.doi.org/10.1016/j.epsl.2011.03.032.

Hoernle K., van den Bogaard P., Werner R., Lissinna B., Hauff F., Alvarado G. and Garbe-Schönberg D. (2002) Missing history (16–71 Ma) of the Galápagos hotspot: implications for the tectonic and biological evolution of the Americas. *Geology* **30**(9), 795–798. http://dx.doi.org/10.1130/0091-7613(2002)030<0795:MHMOTG>2.0.CO;2.

Hoorn C., Wesselingh F. P., ter Steege H., Bermudez M. A., Mora A., Sevink J., Sanmartín I., Sanchez-Meseguer A., Anderson C. L., Figueiredo J. P., Jaramillo C., Riff D., Negri F. R., Hooghiemstra H., Lundberg J., Stadler T., Särkinen T. and Antonelli A. (2010) Amazonia through time: andean uplift, climate change, landscape evolution, and biodiversity. *Science* **330**(6006), 927–931. http://dx.doi.org/10.1126/science.1194585.

Hovan S. A. (1995) Late cenozoic atmospheric circulation intensity and climatic history recorded by eolian deposition in the eastern equatorial pacific ocean, Leg 138. In *Proceedings of the Ocean Drilling Program, 138 Scientific Results*, vol. 138 (eds. N. G. Pisias, L. A. Mayer, T. R. Janecek, A. Palmer-Julson and T. H. van Andel).

Hovikoski J., Wesselingh F. P., Räsänen M., Gingras M. and Vonhof H. B. (2010) Marine influence in Amazonia: evidence from the geological record. In *Amazonia: Landscape and Species Evolution* (eds. C. Hoorn and F. P. Wesselingh), pp. 143–161. Ocean Drilling Program. Wiley-Blackwell Publishing Ltd, Oxford, UK.

Hyeong K., Park S.-H., Yoo C. M. and Kim K.-H. (2005) Mineralogical and geochemical compositions of the eolian dust from the northeast equatorial Pacific and their implications on paleolocation of the Intertropical Convergence Zone. *Paleoceanography* **20**(1), 1–11. http://dx.doi.org/10.1029/2004PA001053.

Janis C. M. (1993) Tertiary mammal evolution in the context of changing climates, vegetation, and tectonic events. *Annu. Rev. Ecol. Syst.* **24**, 467–500.

Jiang S. and Wise S. W. (2007) Upper Cenozoic calcareous nannofossil biostratigraphy and inferred sedimentation, ODP Leg 206, East Pacific Rise. In *Proceedings of the Ocean Drilling Program, 206 Scientific Results*, vol. 206 (eds. D. A. H. Teagle, D. S. Wilson, G. D. Acton and D. Vanko).

Johnson C. M. and Beard B. L. (1999) Correction of instrumentally produced mass fractionation during isotopic analysis of Fe by thermal ionization mass spectrometry. *Int. J. Mass Spectrom.* **193**, 87–99.

Jones C. E., Halliday A. N., Rea D. K. and Owen R. M. (2000) Eolian inputs of lead to the North Pacific. *Geochim. Cosmochim. Acta* **64**(8), 1405–1416. http://dx.doi.org/10.1016/S0016-7037(99)00439-1.

Kerr A. C., Tarney J., Marriner G. F., Nivia A. and Saunders A. D. (1997) The Caribbean-Colombian Cretaceous Igneous Province. The Internal Anatomy of an Oceanic Plateau. In *Large Igneous Provinces, Continental, Oceanic, and Planetary Flood Volcanism, Geophyisical Monograph (100)* (eds. J. J. Mahoney and M. F. Coffin). American Geophysical Union, Washington, pp. 123–144.

Kessler W. S. (2006) The circulation of the eastern tropical Pacific: a review. *Prog. Oceanogr.* **69**(2–4), 181–217. http://dx.doi.org/10.1016/j.pocean.2006.03.009.

Kirby M. X. and MacFadden B. J. (2005) Was Central America an archipelago or a peninsula in the middle Miocene? A text using land-mammal body size. *Paleogeogr. Palaeoclimatol. Palaeoecol.* **228**, 193–202. http://dx.doi.org/10.1016/j.palaeo.2005.06.002.

Kuritani T. and Nakamura E. (2002) Precise isotope analysis of nanogram-level Pb for natural rock samples without use of double spikes. *Chem. Geol.* **186**, 31–43.

Ling H.-F., Jiang S.-Y., Frank M., Zhou H.-Y., Zhou F., Lu Z.-L., Chen X.-M., Jiang Y.-H. and Ge C.-D. (2005) Differing controls over the Cenozoic Pb and Nd isotope evolution of deepwater in the central North Pacific Ocean. *Earth Planet. Sci. Lett.* **232**(3–4), 345–361. http://dx.doi.org/10.1016/j.epsl.2004.12.009.

Lonsdale P. (1976) Abyssal circulation of the southeastern Pacific and some geological implications. *J. Geophys. Res. Oceans* **81**(6), 1163–1176. http://dx.doi.org/10.1029/JC081i006p01163.

Lourens L., Hilgen F., Shackleton N. J., Laskar J. and Wilson D. S. (2004) The Neogene Period. In *A Geological Time Scale 2004* (eds. F. Gradstein, J. Ogg and A. Smith). Cambridge University Press, pp. 409–440.

Lucassen F., Escayola M., Franz G., Romer R. L. and Koch K. (2002) Isotopic composition of late Mesozoic basic and ultrabasic rocks from Andes, 23–32o S)–implications for the Andean mantle. *Contrib. Mineral. Petrol.* **143**(3), 336–349. http://dx.doi.org/10.1007/s00410-001-0344-3.

Lupton J. E. (1995) Hydrothermal plumes: Near and far field. In *Seafloor Hydrothermal Systems: Physical, Chemical, Biological, and Geological Interactions*, vol. 91 (eds. R. A. Humphris, L. S. Mullineaux and Thomson). American Geophysical Union, Washington, DC, pp. 317–346.

Lupton J. E. and Craig H. (1981) A major helium-3 source at 15 S on the East Pacific Rise. *Science* **214**(4516), 13–18. http://dx.doi.org/10.1126/science.214.4516.13.

Lupton J. E., Pyle D. G., Jenkins W. J., Greene R. and Evans L. (2004) Evidence for an extensive hydrothermal plume in the Tonga–Fiji region of the South Pacific. *Geochem. Geophys. Geosyst.* **5**(1). http://dx.doi.org/10.1029/2003GC000607.

Lyle M. (1992) Composition maps of surface sediments of the eastern tropical Pacific Ocean. In *Proceedings of the Ocean Drilling Program, 138 Initial Reports*, vol. 138 (eds. L. Mayer, N. Pisias and T. Janecek), pp. 101–115. Ocean Drilling Program.

Martiny B., Martínez-Serrano R. G., Morán-Zenteno D. J., Macías-Romo C. and Ayuso R. A. (2000) Stratigraphy, geochemistry and tectonic significance of the Oligocene magmatic rocks of western Oaxaca, southern Mexico. *Tectonophysics* **318**, 71–98. http://dx.doi.org/10.1016/S0040-1951(99)00307-8.

Milliman J. D. and Syvitski J. P. M. (1992) Geomorphic/tectonic control of sediment discharge to the ocean: the importance of small mountainous rivers. *J. Geol.* **100**(5), 525–544. http://dx.doi.org/10.1086/629606.

Molnar P. (2008) Closing of the Central American seaway and the ice age: a critical review. *Paleoceanography* **23**(2), 1–15. http://dx.doi.org/10.1029/2007PA001574.

Montes C., Cardona A., McFadden R., Morón S. E., Silva C. A., Restrepo-Moreno S., Ramírez D. A., Hoyos N., Wilson J., Farris D., Bayona G. A., Jaramillo C. A., Valencia V., Bryan J. and Flores J. A. (2012a) Evidence for middle Eocene and younger land emergence in central Panama: implications for Isthmus closure. *Geol. Soc. Am. Bull.* **124**(5–6), 780–799. http://dx.doi.org/10.1130/B30528.1.

Montes C., Bayona G., Cardona A., Buchs D. M., Silva C. A., Morón S., Hoyos N., Ramírez D. A., Jaramillo C. A. and Valencia V. (2012b) Arc-continent collision and orocline formation: closing of the Central American seaway. *J. Geophys. Res. Solid Earth* **117**(B4), 1–25. http://dx.doi.org/10.1029/2011JB008959.

Montes C., Cardona A., Jaramillo C., Pardo A., Silva J. C., Valencia V., Ayala C., Pérez-Angel L. C., Rodriguez-Parra L. A., Ramirez V. and Niño H. (2015) Middle Miocene closure of the Central American Seaway. *Science* **348**(6231), 226–229. http://dx.doi.org/10.1126/science.aaa2815.

Montgomery D. R., Balco G. and Willett S. D. (2001) Climate, tectonics, and the morphology of the Andes. *Geology* **29**, 579–582. http://dx.doi.org/10.1130/0091-7613(2001)029<0579:CTATMO>2.0.CO;2.

Morán-Zenteno D. J., Corona-Chavez P. and Tolson G. (1996) Uplift and subduction erosion in Southwestern Mexico since the Oligocene: pluton geobarometry constraints. *Earth Planet. Sci. Lett.* **141**, 51–65. http://dx.doi.org/10.1016/0012-821X(96)00067-2.

Morán-Zenteno D. J., Tolson G., Martínez-Serrano R. G., Martiny B., Schaaf P., Silva-Romo G., Macías-Romo C., Alba-Aldave L., Hernández-Bernal M. S. and Solís-Pichardo G. N. (1999) Tertiary arc-magmatism of the Sierra Madre del Sur, Mexico, and its transition to the volcanic activity of the Trans-Mexican Volcanic Belt. *J. S. Am. Earth Sci.* **12**(6), 513–535. http://dx.doi.org/10.1016/S0895-9811(99)00036-X.

Nakai S., Halliday A. N. and Rea D. K. (1993) Provenance of dust in the Pacific Ocean. *Earth Planet. Sci. Lett.* **119**(1–2), 143–157. http://dx.doi.org/10.1016/0012-821X(93)90012-X.

O'Dea A., Hoyos N., Rodríguez F., Degracia B. and de Gracia C. (2012) History of upwelling in the Tropical Eastern Pacific and the paleogeography of the Isthmus of Panama. *Palaeogeogr. Palaeoclimatol. Palaeoecol.* **348–349**, 59–66. http://dx.doi.org/10.1016/j.palaeo.2012.06.007.

O'Nions R. K., Carter S. R., Cohen R. S., Evensen N. M. and Hamilton P. J. (1978) Pb, Nd and Sr isotopes in oceanic ferromanganese deposits and ocean floor basalts. *Nature* **273**(5662), 435–438. http://dx.doi.org/10.1038/273435a0.

Patino L. C., Carr M. J. and Feigenson M. D. (2000) Local and regional variations in Central American arc lavas controlled by variations in subducted sediment input. *Contrib. Miner. Petrol.* **138**(3), 265–283. http://dx.doi.org/10.1007/s004100050562.

Pettke T., Halliday A. N., Hall C. M. and Rea D. K. (2000) Dust production and deposition in Asia and the North Pacific Ocean over the past 12 Myr. *Earth Planet. Sci. Lett.* **178**(3–4), 397–413. http://dx.doi.org/10.1016/S0012-821X(00)00083-2.

Pettke T., Halliday A. N. and Rea D. K. (2002) Cenozoic evolution of Asian climate and sources of Pacific seawater Pb and Nd derived from eolian dust of sediment core LL44-GPC3. *Paleoceanography* **17**(3), 1–13. http://dx.doi.org/10.1029/2001PA000673.

Pichat S., Abouchami W. and Galer S. J. G. (2014) Lead isotopes in the Eastern Equatorial Pacific record Quaternary migration of the South Westerlies. *Earth Planet. Sci. Lett.* **388**, 293–305. http://dx.doi.org/10.1016/j.epsl.2013.11.035.

Pound M. J., Haywood A. M., Salzmann U., Riding J. B., Lunt D. J. and Hunter S. J. (2011) A Tortonian (Late Miocene, 11.61–7.25Ma) global vegetation reconstruction. *Palaeogeogr. Palaeoclimatol. Palaeoecol.* **300**(1–4), 29–45. http://dx.doi.org/10.1016/j.palaeo.2010.11.029.

Pound M. J., Haywood A. M., Salzmann U. and Riding J. B. (2012) Global vegetation dynamics and latitudinal temperature gradients during the Mid to Late Miocene (15.97–5.33Ma). *Earth Sci. Rev.* **112**(1–2), 1–22. http://dx.doi.org/10.1016/j.earscirev.2012.02.005.

Rea D. K. (1990) Aspects of atmospheric circulation: the late Pleistocene (0–950,000 yr) record of eolian deposition in the Pacific Ocean. *Palaeogeogr. Palaeoclimatol. Palaeoecol.* **78**(3–4), 217–227. http://dx.doi.org/10.1016/0031-0182(90)90215-S.

Rea D. K. (1994) The paleoclimatic record provided by eolian deposition in the deep sea: The geologic history of wind. *Rev. Geophys.* **32**(2), 159–195. http://dx.doi.org/10.1029/93RG03257.

Rech J. A., Currie B. S., Michalski G. and Cowan A. M. (2006) Neogene climate change and uplift in the Atacama Desert, Chile. *Geology* **34**(9), 761. http://dx.doi.org/10.1130/G22444.1.

Rech J. A., Currie B. S., Shullenberger E. D., Dunagan S. P., Jordan T. E., Blanco N., Tomlinson A. J., Rowe H. D. and Houston J. (2010) Evidence for the development of the Andean rain shadow from a Neogene isotopic record in the Atacama Desert, Chile. *Earth Planet. Sci. Lett.* **292**(3–4), 371–382. http://dx.doi.org/10.1016/j.epsl.2010.02.004.

Rogers R. D., Kárason H. and van der Hilst R. (2002) Epeirogenic uplift above a detached slab in northern Central America. *Geology* **30**, 1031–1034. http://dx.doi.org/10.1130/0091-7613(2002)030<1031:EUAADS>2.0.CO;2.

Rogers R. D., Mann P. and Emmet P. A. (2007) Tectonic terranes of the Chortis block based on integration of regional aeromagnetic and geologic data. In *Special Paper 428: Geologic and Tectonic Development of the Caribbean Plate Boundary in Northern Central America*, vol. 428, pp. 65–88. Special Paper 428: Geologic and Tectonic Development of the Caribbean Plate Boundary in Northern Central America. Geological Society of America.

Schaule B. K. and Patterson C. C. (1981) Lead concentrations in the northeast Pacific: evidence for global anthropogenic perturbations. *Earth Planet. Sci. Lett.* **54**(1), 97–116. http://dx.doi.org/10.1016/0012-821X(81)90072-8.

Shiki T., Yamazaki T. and Hisatomi K. (1982) Features of grain-size distribution and mineral composition of turbiditic sediments from Middle America Trench off Guatemala. DSDP Leg 67. In *Init. Repts. DSDP, 67* (eds. J. Aubouin and R. von Huene). U.S. Govt. Printing Office, Washington, pp. 537–548. http://dx.doi.org/10.2973/dsdp.proc.67.121.1982.

Sims K. W. W., Goldstein S. J., Blichert-Toft J., Perfit M. R., Kelemen P., Fornari D. J., Michael P., Murrell M. T., Hart S. R., DePaolo D. J., Layne G., Ball L., Jull M. and Bender J. (2002) Chemical and isotopic constraints on the generation and transport of magma beneath the East Pacific Rise. *Geochim. Cosmochim. Acta* **66**(19), 3481–3504. http://dx.doi.org/10.1016/S0016-7037(02)00909-2.

Stancin A. M., Gleason J. D., Rea D. K., Owen R. M., Moore, Jr., T. C., Blum J. D. and Hovan S. A. (2006) Radiogenic isotopic mapping of late Cenozoic eolian and hemipelagic sediment distribution in the east-central Pacific. *Earth Planet. Sci. Lett.* **248**(3–4), 840–850. http://dx.doi.org/10.1016/j.epsl.2006.06.038.

Stern C. R. (2004) Active Andean volcanism: its geologic and tectonic setting. *Andean Geology (formerly Revista Geológica de Chile)* **31**(2), 161–206. http://dx.doi.org/10.5027/andgeoV31n2-a01.

Stumpf R., Frank M., Schönfeld J. and Haley B. A. (2010) Late Quaternary variability of Mediterranean Outflow Water from radiogenic Nd and Pb isotopes. *Quatern. Sci. Rev.* **29**(19–20), 2462–2472. http://dx.doi.org/10.1016/j.quascirev.2010.06.021.

Thirlwall M. F. (2000) Inter-laboratory and other errors in Pb isotope analyses investigated using a ^{207}Pb–^{204}Pb double spike. *Chem. Geol.* **163**, 299–322.

Thirlwall M. F. (2002) Multicollector ICP-MS analysis of Pb isotopes using a ^{207}Pb–^{204}Pb double spike demonstrates up to 400 ppm/amu systematic errors in Tl-normalization. *Chem. Geol.* **184**, 255–279.

van de Flierdt T., Frank M., Halliday A. N., Hein J. R., Hattendorf B., Günther D. and Kubik P. W. (2004a) Deep and bottom water export from the Southern Ocean to the Pacific over the past 38 million years. *Paleoceanography* **19**(1), PA1020. http://dx.doi.org/10.1029/2003PA000923.

van de Flierdt T., Frank M., Halliday A. N., Hein J. R., Hattendorf B., Günther D. and Kubik P. W. (2004b) Tracing the history of submarine hydrothermal inputs and the significance of hydrothermal hafnium for the seawater budget—a combined Pb–Hf–Nd isotope approach. *Earth Planet. Sci. Lett.* **222**(1), 259–273. http://dx.doi.org/10.1016/j.epsl.2004.02.025.

von Blanckenburg F. and Igel H. (1999) Lateral mixing and advection of reactive isotope tracers in ocean basins: observations and mechanisms. *Earth Planet. Sci. Lett.* **169**(1–2), 113–128. http://dx.doi.org/10.1016/S0012-821X(99)00070-9.

von Blanckenburg F., O'Nions R. K. and Heinz J. R. (1996) Distribution and sources of pre-anthropogenic lead isotopes in deep ocean water from Fe–Mn crusts. *Geochim. Cosmochim. Acta* **60**(24), 4957–4963. http://dx.doi.org/10.1016/S0016-7037(96)00310-9.

von Huene R. and Aubouin J., et al. (1982) Site 495: Cocos Plate Middle America Trench Outer Slope. In *Initial Reports of the Deep Sea Drilling Project, 67*, vol. 67 (eds. J. Aubouin and R. von Huene). Government Printing Office, US, pp. 79–141.

Waters C. L., Sims Kenneth W. W., Perfit M. R., Blichert-Toft J. and Blusztajn J. (2011) Perspective on the genesis of E-MORB from Chemical and Isotopic Heterogeneity at 9–10 N East Pacific Rise. *J. Petrol.* **52**(3), 565–602. http://dx.doi.org/10.1093/petrology/egq091.

Werner R. and Hoernle K. (2003) New volcanological and volatile data confirm the hypothesis for the continuous existence of Galápagos Islands for the past 17 m.y. *Int. J. Earth Sci.* **92**(6), 904–911. http://dx.doi.org/10.1007/s00531-003-0362-7.

Werner R., Hoernle K., van den Bogaard P., Ranero C., von Huene R. and Korich D. (1999) Drowned 14-m.y.-old Galápagos archipelago off the coast of Costa Rica: Implications for evolutionary and tectonic models. *Geology* **27**(6), 499–502. http://dx.doi.org/10.1130/0091- 7613(1999)027<0499:DMYOGP>2.3.CO;2.

Webb S. D. (1977) A history of savanna vertebrates in the new world. Part I: North America. *Annu. Rev. Ecol. Syst.* **8**, 355–380.

Webb S. D. (1978) A history of Savanna Vertebrates in the New World. Part II: South America and the great interchange. *Annu. Rev. Ecol. Syst.* **9**(1), 393–426. http://dx.doi.org/10.1146/annurev.es.09.110178.002141.

Whitmore, Jr., F. C. and Stewart R. H. (1965) Miocene mammals and Central American seaways. *Science* **148**, 180–185. http://dx.doi.org/10.1126/science.148.3667.180.

Wilson D. S. (1996) Fastest known spreading on the Miocene Cocos-Pacific Plate Boundary. *Geophys. Res. Lett.* **23**(21), 3003–3006. http://dx.doi.org/10.1029/96GL02893.

Wilson D. S., Teagle D. A. H. and Acton G. D., et al. (2003) Site 1256, preliminary results. In *Proceedings of the Ocean Drilling Program, 206 Initial Reports*, vol. 206 (eds. D. Wilson, D. Teagle and G. Acton).

Wilson D. J., Galy A., Piotrowski A. M. and Banakar V. K. (2015) Quaternary climate modulation of Pb isotopes in the deep Indian Ocean linked to the Himalayan chemical weathering. *Earth Planet. Sci. Lett.* **424**, 256–268.

Woodburne M. O. (2010) The Great American biotic interchange: dispersals, tectonics, climate, sea level and holding pens. *J. Mammalian Evol.* **17**(4), 245–264. http://dx.doi.org/10.1007/s10914-010-9144-8.

Wyrtki K. and Kilonsky B. (1984) Mean water and current structure during the Hawaii-to-Tahiti shuttle experiment. *J. Phys. Oceanogr.* **14**(2), 242–254. http://dx.doi.org/10.1175/1520-0485(1984)014<0242:MWACSD>2.0.CO;2.

Xie R. C. and Marcantonio F. (2012) Deglacial dust provenance changes in the Eastern Equatorial Pacific and implications for ITCZ movement. *Earth Planet. Sci. Lett.* **317–318**, 386–395. http://dx.doi.org/10.1016/j.epsl.2011.11.014.

Associate editor: Janne Blichert-Toft